

# TrajectoryFlowNet: Hybrid Lagrangian–Eulerian learning of flow field and trajectories

Jingdi Wan<sup>1</sup>, Hongping Wang<sup>2</sup>, Bo Liu<sup>1</sup>, Guowei He<sup>1,2</sup>, Yang Liu<sup>1,2\*</sup>

<sup>1</sup>School of Engineering Science, University of Chinese Academy of Sciences, Beijing, China

<sup>2</sup>Institute of Mechanics, Chinese Academy of Sciences, Beijing, China

\*Corresponding authors

## Abstract

The process of flows carrying particles is highly complex, traditionally tackled by solving the Navier-Stokes equations. Although different numerical and experimental techniques have been developed, these approaches demand a deep understanding of the underlying physics and are frequently associated with high computational costs. Machine learning offers a novel alternative, learning predictive patterns directly from data, thus bypassing the need for explicit physical modeling. Nonetheless, pure data-driven methods can sometimes lack interpretability and physical consistency. By integrating physics principles into machine learning, this gap can be bridged and the above problems can be solved. In this context, we have proposed TrajectoryFlowNet for flow and particle tracking. Our approach combines the flexibility of data-driven learning with the rigorousness of physics-based constraints, aiming to achieve both accuracy and efficiency. The salient features of our model include its ability to handle complex flow patterns with moving boundaries, predict the trajectories of all particles in the domain, and ensure physical consistency throughout the predictions based only on sparse trajectories. To validate our method, we have conducted several numerical and experimental cases across a range of flow scenarios. These experiments demonstrate the model’s effectiveness in capturing the intricate dynamics of particle-laden flows, advancing precise particle tracking and flow field inversion in various real-world problems.

**Keywords:** machine learning, passive particle, trajectory tracking, flow field prediction

## Introduction

Tracking and quantifying fluid flow plays an important role in many nature and engineering applications, e.g. physics, oceanography, ecology, and pharmacokinetics [9, 10, 16, 31]. In such a process, the flow state is tracked using small particles, or tracer particles, that are passively transported [48]. By assuming that the particle behaves as an infinitesimal fluid element, the flow properties can be better understood, analyzed and predicted. However, the complexity associated with solving the Navier-Stokes equations present significant challenges that are inherently difficult to address directly [28].

Experimental techniques such as Particle Image Velocimetry (PIV) and drifters have proven to be effective and accurate in capturing flow information for small-scale and mesoscale fluid dynamics, respectively [70, 71]. PIV necessitates high-quality and uniformly dense particles as tracking markers,

which may limit its applicability in scenarios involving low-density or specialized gases [69]. While PIV enables the acquisition of velocity distribution within the flow field, it presents challenges in obtaining the density distribution, thereby impeding the construction of the pressure field using this method [25]. In recent years, advancements in positioning and data transmission technologies have significantly enhanced the utility of drifters as experimental tools for measuring mesoscale vortices. Nevertheless, the spatial domain covered by drifters often proves inadequate for comprehensive flow analysis, and the data obtained through drifters may be sparse for many practical problems [4]. In the biomedical field, nanoparticle-based *in vivo* imaging has been extensively studied over the past few decades. Nanoparticles can readily incorporate multiple imaging or therapeutic agents, offering potential for personalized medicine as passive transport carriers. However, existing *in vivo* imaging techniques such as near-infrared fluorescence imaging, magnetic resonance imaging, and ultrasound imaging face intrinsic limitations. These include insufficient resolution and the inability to explicitly capture trajectories of passive particles, which ultimately constrain the acquisition of accurate and reliable information at the disease site [76, 77].

The numerical approach enables the characterization of flow states by tracking passive particles within the fluid through the solution of discrete partial differential equations [21]. Among them, Lagrangian particle tracking, based on the flow characteristics obtained by the hydrodynamic model, is an important tool in quantifying the flow transmission in fluid [48–52]. This method serves as a valuable tool for investigating the behavior and transport properties of particles in fluid systems. By tracking the trajectories of Lagrangian particles, which represent fluid elements, a comprehensive analysis of fluid motion and comprehension of intricate flow phenomena can be achieved [53]. However, the number of particles tracked becomes the main obstacle to the use of this method. As the number of particles increases, the computational resources required also increase significantly. Meanwhile, Lagrangian particle tracking is computationally slow in unstructured grids, which greatly limits the number of particles actually tracked and the range of behaviors that can be modeled [54–61].

The rapid advancement of computing hardware and the availability of vast amounts of big data have revolutionized the field of artificial intelligence, making it an exceptionally powerful tool for constructing data-driven models [3, 6, 7]. In the realm of fluid mechanics, leveraging the extensive collection of experimental observations and numerical simulation data has emerged as a novel approach to deep learning algorithms, enabling the development of innovative solutions for fluid flow problems [17, 21, 41]. Traditional deep learning methods heavily rely on rich labeled datasets. Due to the over-parameterized and black-box nature of the models, issues arise in interpretability, overfitting, and generalization. Embedding existing knowledge in the field of fluid mechanics to form data and physics learning has shown potential in alleviating these fundamental issues, leading to the generation of more robust models for reliable predictions.

Physics-Informed Neural Network (PINN) have been proposed as a solution for both forward and inverse problems associated with partial differential equations [73]. By integrating known physical information with data, PINN significantly reduce the reliance on large volumes of training data, leading to faster convergence and improved prediction accuracy of the neural network [11, 14]. PINN possess inherent advantages in addressing challenges related to incomplete physical information and limited training data, making them highly regarded in the field of fluid mechanics. For instance, the HFM model successfully predicted flow states from concentration measurements at discrete sampling points [78]. Chen et al. [79] applied PINN to identify the functional forms of governing equations, including the Navier–Stokes equations. Wang et al. [80] used PINN to reconstruct high-resolution velocity fields from sparse particle image velocimetry (PIV) data, while Cai et al. [81] developed the AIV method to quantify hemodynamic velocity and stress fields. Although these methods produce flow fields that are consistent with PIV observations, they lack explicit treatment

of Lagrangian particle dynamics. Specifically, Wang’s approach does not incorporate tracer-particle trajectory tracking, and although AIV captures variations in particle velocities, it does not yield explicit particle trajectories. These limitations motivated us to develop a novel network architecture capable of simultaneously predicting passive particle trajectories and inferring the underlying flow field, offering a more comprehensive and physically consistent description of fluid motion.

To this end, we leverage recent advances to present TrajectoryFlowNet, an innovative approach for flow and particle tracking based on sparse trajectory data. This method combines the flexibility of data-driven learning with the precision of physics-based constraints, aiming to achieve high accuracy and computational efficiency. Our model is designed with notable features such as interpretability, generalizability, and physical consistency. Specifically, TrajectoryFlowNet integrates several key innovations: (1) a hybrid approach combining Lagrangian and Eulerian descriptions that enables comprehensive reconstruction of both individual trajectories and continuum flow dynamics, enhancing the robustness and versatility of the predictions; (2) Fourier feature mapping overcomes spectral bias in neural networks, enabling accurate learning of high-frequency functions in low-dimensional problems and enhancing the capability to model complex, unsteady, and highly viscous flows such as blood circulation; and (3) guaranteed physical consistency through the incorporation of physics-informed constraints, ensuring that the learned dynamics adhere to fundamental principles. Unlike traditional PINN, our network integrates a sequential prediction framework that guarantees the forward propagation strictly conforms to the physical process. By incorporating physical constraints derived from the Navier-Stokes equations into the learning process, our approach ensures that all predicted trajectories adhere to the fundamental laws of fluid mechanics, significantly enhancing both reliability and accuracy. Through extensive experiments and evaluations, we demonstrate the effectiveness of TrajectoryFlowNet in accurately tracking particles in various flow scenarios. Our approach not only achieves high prediction accuracy but also offers computational efficiency, making it a promising tool for practical applications in fluid dynamics research and engineering.

## Results

### Hybrid Lagrangian–Eulerian Modeling of Flow Trajectories

We examine a fluid parcel composed of microscopic particles. The size of the fluid inclusions is significant enough to retain average meaning, yet small compared to the macroscopic flow length scale, effectively treated as a point, or a passive particle. We assume that the process initiates from the reference configuration and evolves into its morphing configuration. This transformation is mathematically formalized as a mapping from the reference coordinate system to the Eulerian coordinate system, termed a flow graph, written as:

$$\mathbf{X}(\cdot, t) : \mathbb{R}^d \rightarrow \mathbb{R}^d \quad \text{and} \quad \mathbf{X}(\cdot, 0) = \text{identity map}, \quad (1)$$

where  $\mathbf{x} = \mathbf{X}(\boldsymbol{\xi}, t)$  is the spatial location of the parcel  $\boldsymbol{\xi} \in \mathbb{R}^d$  in  $d$ -dimensional Eulerian coordinate at time  $t \in \mathbb{R}^+$ . The map is one-to-one, continuous, and differentiable, allowing us to write  $\boldsymbol{\xi} = \boldsymbol{\xi}(\mathbf{x}, t) := \mathbf{X}^{-1}(\mathbf{x}, t)$ . Here  $\mathbf{X}^{-1}(\cdot, t) : \mathbb{R}^d \rightarrow \mathbb{R}^d$  is the map from Eulerian coordinate back to the reference coordinate. We use  $\mathbf{x}$  for the mapping  $\mathbf{X}$  to simplify the notation, treating the change from Eulerian to Lagrangian coordinate as a variable change. To facilitate the distinction between physical quantities under different descriptions, we employ the notation  $\tau \in \mathbb{R}^+$  to represent the time of independent particle motion in the Lagrangian description, and  $t$  to denote the observation time of the physical field in the Eulerian description. The spatial location of the parcel is given by:

$$\mathbf{x} = \mathbf{x}(\boldsymbol{\xi}, \tau), \quad (2)$$

where  $\tau = t - t_0$ ,  $t_0 \in \mathbb{R}^+$  represents the corresponding initial motion time. With trajectories, the identification is evident as the parcel location is known at any time. We propose to identify each parcel by referring to its initial location  $\mathbf{x}_0 \in \mathbb{R}^d$  and initial motion time  $t_0$ , i.e.,  $\mathbf{x} = \mathbf{x}(\boldsymbol{\xi}, \tau) = \mathbf{x}(\mathbf{x}_0, \tau_0, \tau)$ . It is an Eulerian vector field, which will be treated directly within the Eulerian model.

To express the physical law composed of partial derivatives, a shift to the Lagrangian coordinate system  $(\mathbf{x}(\boldsymbol{\xi}, \tau), \tau)$  is necessary. By the chain rule,

$$\frac{\partial}{\partial \tau}(f(\mathbf{x}(\boldsymbol{\xi}, \tau), t(\tau))) = \mathbf{u} \cdot \nabla f + f_t, \quad (3)$$

where  $\nabla \in \mathbb{R}^d$  is the Nabla operator,  $\mathbf{u} \in \mathbb{R}^d$  is the parcel velocity vector composed of  $d$  components,  $f_t$  is the time derivative of the functional of  $\mathbf{x}$  and  $t$ . The derivative with respect to the  $\tau$  variable, is given as:

$$D_\tau = \frac{\partial}{\partial \tau} = (\partial_t + \mathbf{u} \cdot \nabla). \quad (4)$$

The Navier-Stokes equation without external forces is written as:

$$\frac{\partial \mathbf{u}}{\partial t} + (\mathbf{u} \cdot \nabla) \mathbf{u} = -\frac{1}{\rho} \nabla p + \frac{\mu}{\rho} \nabla^2 \mathbf{u}, \quad (5)$$

where  $\rho \in \mathbb{R}$  is the density,  $p \in \mathbb{R}$  denotes the pressure. This equation characterizes the fluid motion, incorporating the effects of inertia, pressure, and viscosity.

Our objective is to correlate the initial positions of particles with their trajectories by analyzing measured particle motion trajectories, velocities, and pressures, meanwhile to forecast velocity and pressure changes throughout the flow field using this data, which is typically incomplete, sparse, and noisy in real-world scenarios. This is often the case when data capture is expensive or the data itself is limited. We consider all passive particles as fluid parcels, meaning they can be regarded as part of the fluid. These passive particles can be released at any location and time within the fluid domain. The initial position  $\mathbf{x}_0$  and initial time  $t_0$  distinguish each particle. Consequently, the trajectory  $\mathbf{x}$  of a passive particle can be computed using Eq. (2). Based on the particle trajectories, the fluid velocity  $\mathbf{u}$  and pressure  $p$  along the trajectory can be calculated by  $\mathbf{u} = \mathbf{u}(\mathbf{x}, t)$  and  $p = p(\mathbf{x}, t)$ .

It is important to note that the state variables in these calculations must satisfy corresponding relationships. Specifically, the time derivative of the particle trajectory  $\mathbf{x}$  must equal the velocity at that location, i.e.,

$$\frac{d\mathbf{x}}{d\tau} = \mathbf{u}. \quad (6)$$

Additionally, the predicted velocity and pressure of the flow field must satisfy Eq. (5).

Although the Lagrangian and Eulerian descriptions differ in their mathematical formulations, they essentially represent the same underlying physical state. In light of this, we leverage the flexibility of data-driven methodologies to propose a novel TrajectoryFlowNet paradigm that seamlessly integrates the strengths of both perspectives within a unified algorithmic framework—enabling simultaneous particle trajectory tracking and flow field inference. As illustrated in Fig. 1, this innovative architecture comprises two core components: the Trajectory block and the Flow Field block. Within the Trajectory block, where the objective is to trace particle paths, we naturally adopt the Lagrangian description; conversely, the Flow Field block employs the Eulerian perspective, which proves more effective for characterizing fluid states. Specifically, the predicted particle displacements from the Trajectory block, combined with known initial positions, yield complete particle trajectories. The predicted trajectories  $\mathbf{x}_q \in \mathbb{R}^d$ , along with the corresponding known observation time  $t$  under the Eulerian frame, are fed into the Flow Field block to infer velocity and pressure fields across

space and time. To enhance the network’s capacity to learn this complex functional relationship, we employ Fourier feature mapping at the input of each block, which can significantly improves the model’s ability to resolve high-frequency features in the flow field, thereby enhancing the accuracy of both trajectory and state predictions. Furthermore, using automatic differentiation, we compute the derivative of particle position  $\mathbf{x}_q$  with respect to its motion time variable  $\tau$  at machine precision, as formulated in Eq. (6). The residual between this derivative and the network-predicted velocity is utilized to balance the training dynamics of the two blocks. Additionally, automatic differentiation enables the construction of the Navier–Stokes equations, as formulated in Eq. (5), by enforcing differentiability of the flow field velocity and pressure with respect to spatial coordinates  $\mathbf{x}_q$  and observational time  $t$ . Notably, since measurement data inherently encode specific initial and boundary conditions (I/BCs), these constraints, whether they are a priori known or empirically obtainable, do not need to be explicitly defined during model construction. More details of the TrajectoryFlowNet are given in [Methods](#).

To demonstrate the effectiveness of TrajectoryFlowNet in tracking the long-range trajectories of passive particles and inferring flow field characteristics, we have considered four distinct systems: Lid-Driven Cavity Flow, Complex Cylinder Flow, Aortic Blood Flow, and Left Ventricle Blood Flow. The datasets for the first two systems were obtained by temporally and spatially down sampling high-fidelity numerical simulations that encompass various initial conditions, boundary conditions, number of passive particles, Reynolds numbers, and flow regimes. In contrast, the data for other two system were sourced from real experimental measurements as detailed in the supplementary information. Additional relevant details, including specifics on data generation, can also be found in the supplementary information. During experimentation, we evaluated a variety of comparative methodologies, such as employing different activation functions and using separate networks to predict trajectories and flow fields individually, finding that our proposed approach outperforms existing methods, as elaborated in the supplementary information. Once trained, the model demonstrates its capability to track passive particle movements and infer flow field information within the spatiotemporal domain it was trained on. Comprehensive details regarding the experimental setup, results, and parameter studies of the TrajectoryFlowNet model are provided in the supplementary information.

## Lid-Driven cavity flow

Square cavity flow has been extensively studied by numerous scholars for decades, primarily due to its simple geometric structure and the inclusion of various fluid dynamics phenomena, such as boundary layer separation, cavity vortices, and self-sustained oscillations. Despite these studies, there is still no theoretical model for this classic flow due to its complexity, which makes deriving a theoretical model challenging. These factors have motivated our research interest in applying machine learning methods to model square cavity flow.

We used FLUENT to establish a square cavity with a side length of 1 unit, with fixed left, right, and bottom walls, and a moving top wall. To verify the network’s accuracy, the top lid was moved to the right at an initial speed of  $u = 1$  m/s, corresponding to a Reynolds number of 100. The computational domain was divided into a uniform grid of  $100 \times 100$  as shown in Fig. 2a. Under the influence of the moving top lid, a large vortex formed near the geometric center of the cavity, with smaller flows at the bottom and side edges. At  $t = 3$  s, 300 particles were dispersed inside the cavity, and their trajectories, as well as the velocity and pressure at their locations, were recorded. The total motion duration was 30 seconds. The training set randomly selected 80,200 data points from 200 particles. The test set included 40,100 data points from 100 particles. The dimensionless data were input into the network for training after adding a Fourier feature mapping. The inputs

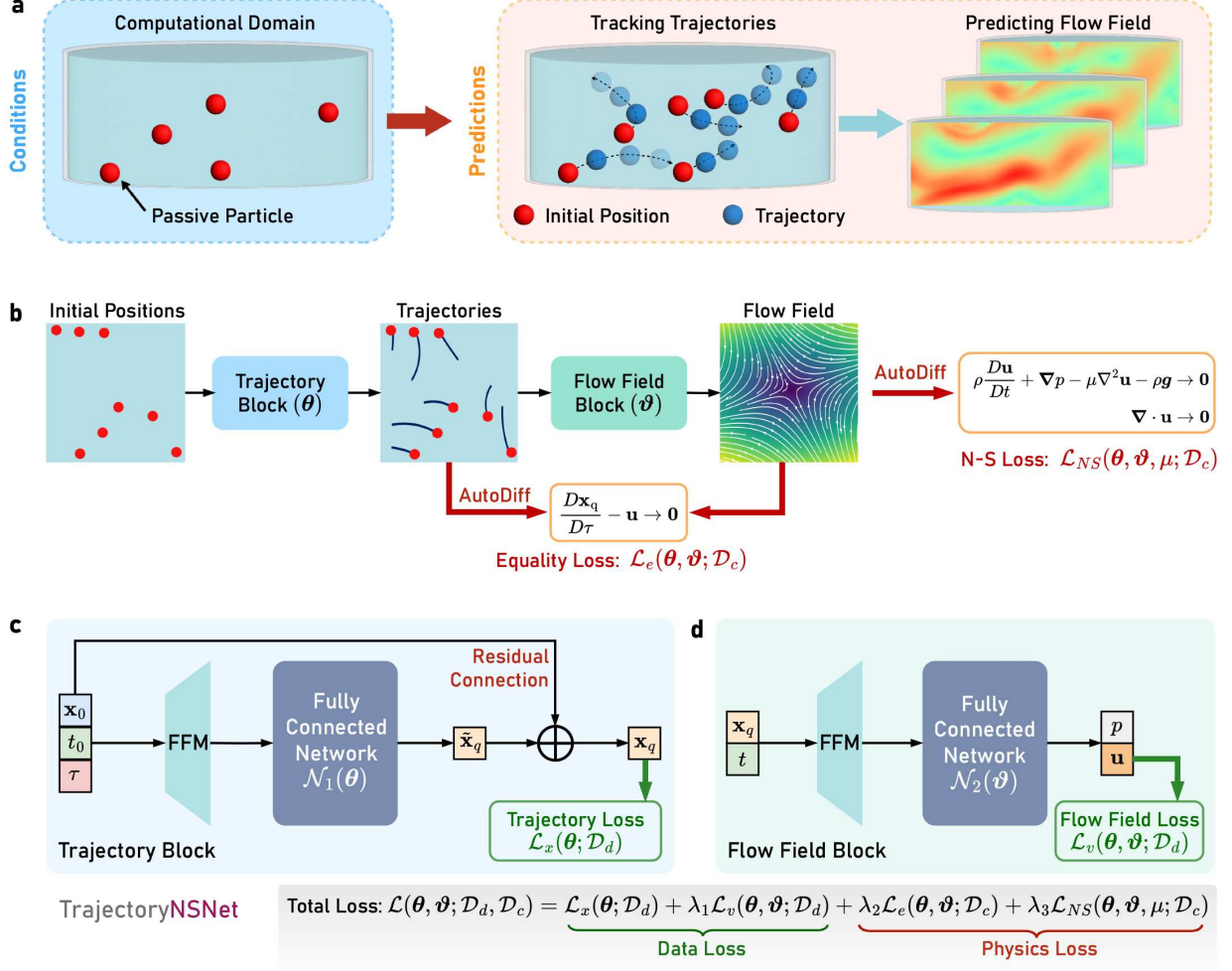


**Figure 1: Overview of TrajectoryFlowNet.** **a**, The computational domain contains only the initial positions of passive particles (red dots), aiming to predict the trajectories of these particles (blue dots) and infer the flow field information. **b**, Schematic architecture of the framework of TrajectoryFlowNet for Modeling Flow Trajectories based on Lagrangian Navier-Stokes Equation. The network consists of Trajectory block and Flow Field block. **c**, The Trajectory block, controlled by trainable parameters  $\theta$ , maps the initial position, release time and motion time  $\mathbf{x}_0, t_0, \tau$  of a particle to its displacement  $\tilde{\mathbf{x}}_q = \tilde{\mathbf{x}}_q(\mathbf{x}_0, t_0, \tau)$  after a Fourier feature mapping  $\gamma_1$ . By adding this displacement to the initial position, we obtain the particle's trajectory  $\mathbf{x}_q = \tilde{\mathbf{x}}_q \oplus \mathbf{x}_0$ . **d**, The Flow Field block, controlled by trainable parameters  $\vartheta$ , uses the Fourier feature-mapped particle trajectories and motion times, predicted by Trajectory block, as input and learns the mapping to the flow field's velocity  $\mathbf{u}$  and pressure  $p$ . Using automatic differentiation, we compute the derivative of the particle position  $\mathbf{x}_q$  with respect to the particle motion time  $\tau$ ,  $\frac{d\mathbf{x}}{d\tau}$ , at machine precision. The residual between this derivative and the network-predicted velocity is used to further balance the training of the two networks. Additionally, automatic differentiation constructs the relationships of flow field velocity and pressure with respect to location and motion time, as described by the Navier-Stokes Equation. The total loss function for training the TrajectoryFlowNet includes data losses  $\mathcal{L}_x$  and  $\mathcal{L}_v$ , as well as residual physics losses  $\mathcal{L}_e$  and  $\mathcal{L}_p$ . Here,  $\mathcal{D}_d$  represents the loss evaluated at data points, and  $\mathcal{D}_c$  represents the loss evaluated at collocation points.

were initial positions  $\mathbf{x}$ , motion times  $\tau$ , and release time  $t_0$ . Collocation points were selected using Latin hypercube sampling, with 160,400 data points in the spatiotemporal domain. The inputs were then transformed using random Gaussian Fourier feature mapping before being fed into the network for training. Optimization was performed using L-BFGS until convergence.

The performance of TrajectoryFlowNet in terms of prediction error across all four cases is sum-



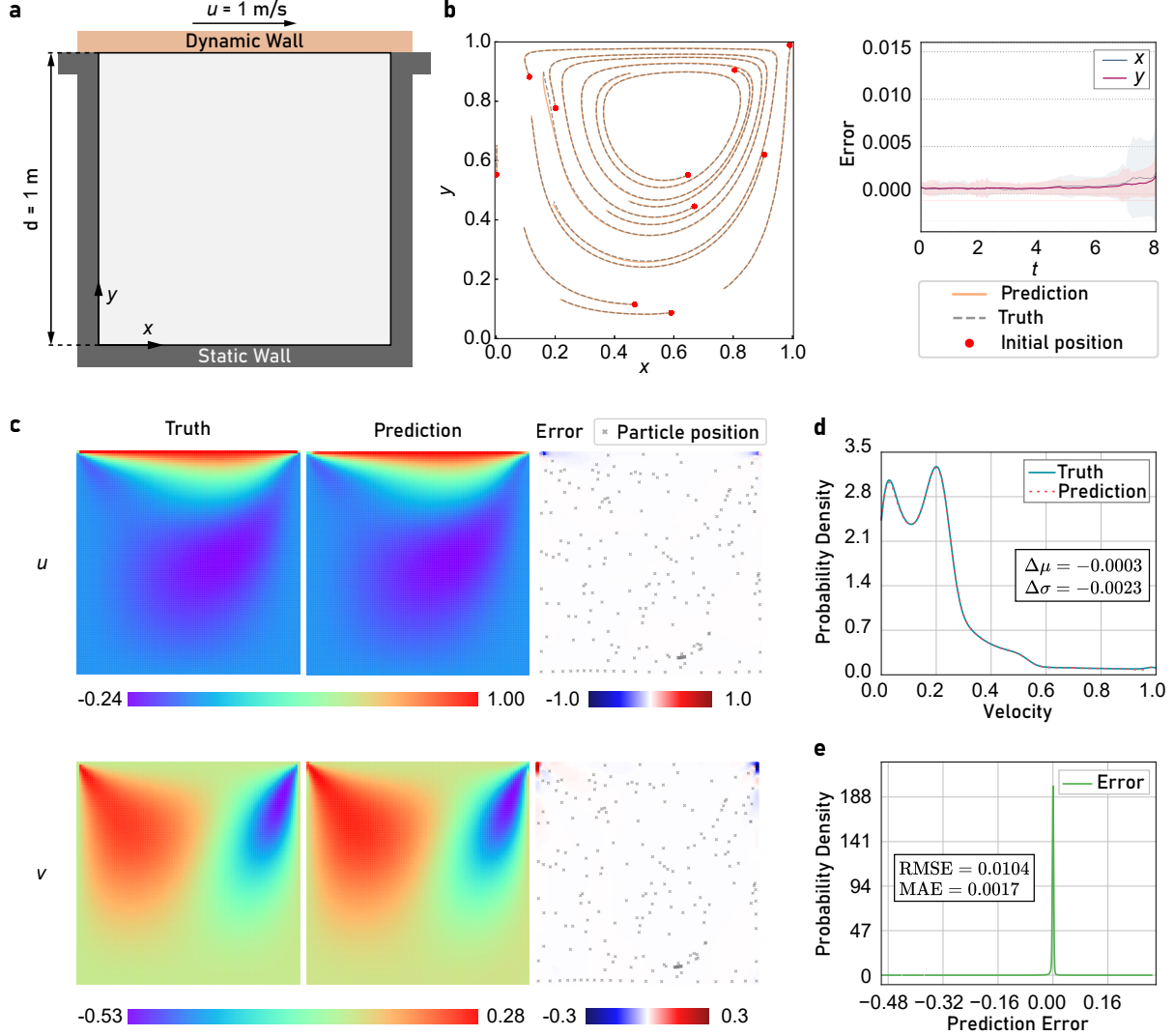


**Figure 2: Establishment of Lid-Driven Cavity Flow Case and Prediction Results.** **a**, Establishment of Lid-Driven Cavity Flow Case. A square cavity model with a side length of 1 unit was established using FLUENT. The top cover moves while the other three sides are fixed. The top cover moves to the right at a velocity of  $u = 1$  m/s, resulting in a flow with a Reynolds number of 100. At  $t = 10$  s, 300 particles are released within the cavity, and their trajectories, velocities, and pressure data are recorded. **b**, Prediction results of particle trajectories for the Lid-Driven Cavity Flow Case. The testing dataset is used to evaluate the network’s ability to predict particle motion trajectories. Selected trajectories predicted by TrajectoryFlowNet are shown, with red dots representing the initial positions of the passive particles. Solid lines represent the predicted trajectories by TrajectoryFlowNet, and dashed lines represent the true values. The right line chart evaluated the performance of TrajectoryFlowNet by measuring the mean (solid line) and standard deviation (shaded region) of the trajectory error over time across all test sequences. **c**, Prediction results of the flow field for the Lid-Driven Cavity Flow Case. The testing dataset is used to evaluate the network’s ability to predict fluid flow states. Snapshots predicted by TrajectoryFlowNet at  $t = 25$  s are presented. The fork symbols in the error plots represent the positions of the training set particles at that moment. **d**, Kernel Density Estimation analysis of velocity fields in the test dataset at  $t = 25$  s. The solid blue line represents the ground truth, the dashed red line denotes the predictions by TrajectoryFlowNet. **e**, Kernel Density Estimation analysis of velocity prediction error in the test dataset at  $t = 25$  s.

marized in Table 1, showcasing the model’s robustness and high accuracy. Fig. 2b displays the pre-

**Table 1:** Summarize the performance of each example in terms of prediction error.

Verifiable Example	Pearson correlation				
	$x$	$y$	$u$	$v$	$p$
Lid-Driven Cavity Flow	0.9999	0.9999	0.9992	0.9989	0.9890
Complex Cylinder Flow	0.9984	0.9872	0.9646	0.9368	0.9457
Experimental Aortic Blood Flow	0.9999	0.9999	0.9554	0.9018	-
Experimental Left Ventricle Blood Flow	0.9986	0.9831	0.7824	0.9286	-

dicted particle trajectories, line chart on the right evaluated the performance of TrajectoryFlowNet by measuring the mean (solid line) and standard deviation (shaded region) of the trajectory error over time across all test sequences. The error remains consistently low throughout the trajectories, with a mean below 0.003 and a standard deviation under 0.0051. Fig. 2d displays the kernel density estimate (KDE) of flow velocity magnitude at  $t = 25$  s, characterizing the distribution of velocities predicted by our algorithm. The blue solid line represents the ground truth, while the red dashed line corresponds to the model predictions. The close alignment between the two curves, together with their sharp peaks and narrow spreads, indicates that the predicted results are closely aligned with the ground truth. Moreover, the absolute differences in mean ( $\Delta\mu$ ) and standard deviation ( $\Delta\sigma$ ) are both below 0.003, further confirming the model’s excellent agreement with the ground truth. KDE of velocity prediction errors at  $t = 25$  s is shown in Fig. 2e, demonstrates that all prediction errors are concentrated around zero. Additionally, both the root mean square error (RMSE) and mean absolute error (MAE) have absolute values less than 0.011.

### Complex cylinder flow

In practical applications, the focus often shifts to unconfined flows, such as river currents, oceanic movements, and atmospheric dynamics, which may also involve internal obstructions that are not fully characterized. To evaluate the generalization capabilities of TrajectoryFlowNet under unconfined domain, we constructed a complex two-dimensional flow scenario around a cylinder, as depicted in Fig. 3a. The cylinder is placed within a duct featuring an inlet and an outlet. FLUENT was utilized with liquid water from its material library as the working fluid. A steady inlet velocity of 0.2 m/s was set, resulting in a Reynolds number of 146,404. Passive tracer particles were uniformly released at the inlet to accurately simulate real-world release conditions. Further details are provided in the subsequent sections.

We trained the TrajectoryFlowNet using the simulated data. Fig. 3b-c illustrate the predicted particle trajectories in test set and flow velocities at  $t = 25$  s. Our model successfully predicts particle motion and flow states based solely on initial positions. The correlation values for velocity and pressure fields exceeded 0.9. Additionally, we derived smooth pressure information that traditional PIV methods cannot directly measure, relying only on the applied physical conditions and the known outlet pressure of 0 Pa. Fig. 3d further analyses the mean (solid line) and standard deviation (shaded region) of trajectory prediction errors for passive particles on the test set. The error remains stable throughout the training time horizon, with a mean below 0.014 and a standard deviation under 0.0021. Kernel density estimates of the predicted velocity fields at  $t = 25$  s are shown in Fig. 3e-f. The negligible shift in mean ( $\Delta\mu = 0.0001$ ) indicates that the model achieves sub-permille-level accuracy ( $< 0.1$  ‰) in the first moment of the velocity distribution, demonstrating that no systematic bias is introduced in the modeling of global momentum conservation. However, a small reduction in the standard deviation ( $\Delta\sigma = -0.0039$ ) suggests a mild smoothing effect on extreme



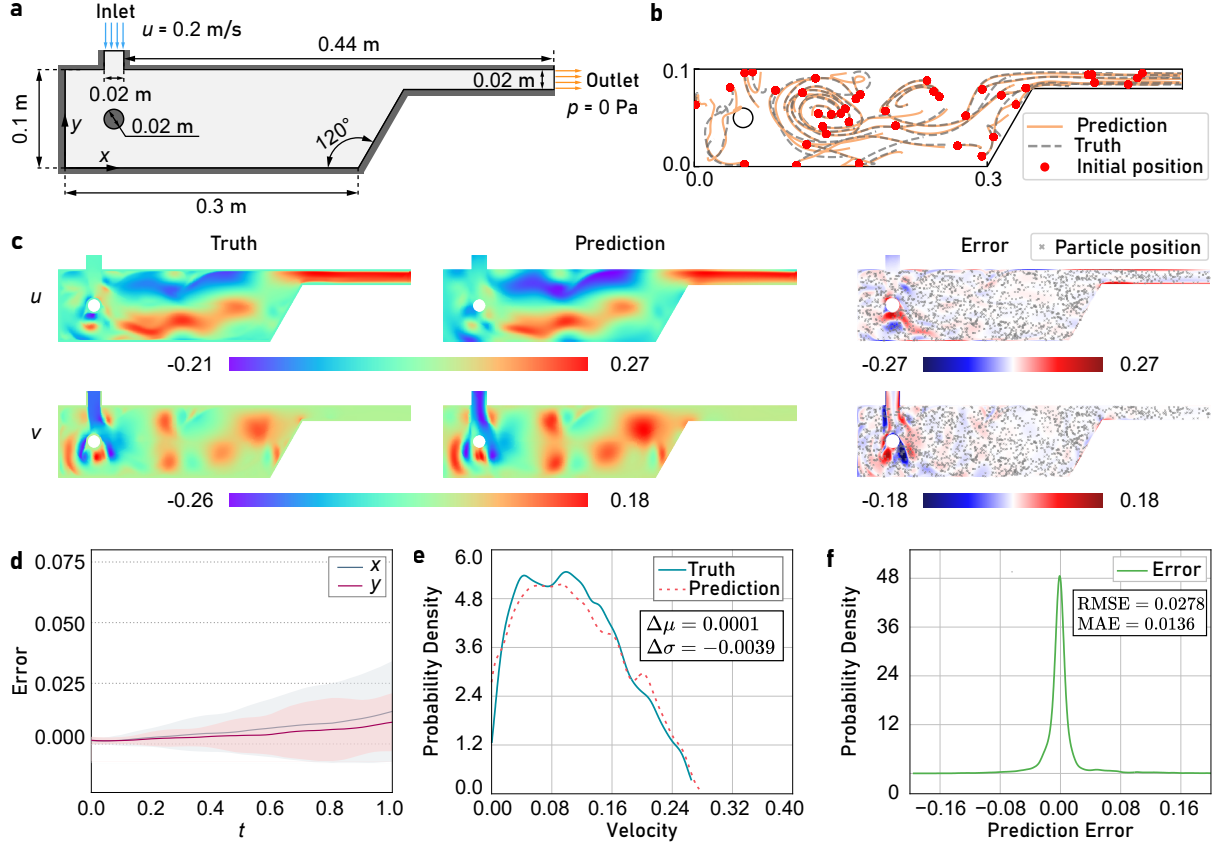


**Figure 3: Establishment of Complex Cylinder Flow Case and Prediction Results.** **a**, Establishment of Complex Cylinder Flow Case. The simulation involves a duct with a stationary cylinder inside, where the cylinder’s diameter matches that of the inlet and outlet. The inlet velocity is set to a constant  $u = 0.2$  m/s, and the outlet pressure is specified as 0 Pa. Using FLUENT software, liquid water from the FLUENT materials library is used as the fluid medium. At  $t = 10$  s, 2200 tracer particles are released at the inlet to track their positions and velocities. **b**, Trajectory prediction results for the Complex Cylinder Flow scenario. The test set is utilized to assess the model’s capability in forecasting particle motion trajectories. Representative predicted trajectories from TrajectoryFlowNet are visualized, with red dots marking the initial positions of the passive particles. Solid lines represent the predicted trajectories by TrajectoryFlowNet, and dashed lines represent the true values. **c**, Prediction results of the flow field for the Complex Cylinder Flow case. The test set is applied to validate the model’s fluid state prediction accuracy. Snapshots predicted by TrajectoryFlowNet at  $t = 25$  s are presented. The fork symbols in the error plots represent the positions of the training set particles at that moment. **d**, Temporal evolution of prediction errors in the test set. Line chart illustrates the performance of TrajectoryFlowNet through temporal analysis of mean (solid line) and standard deviation (shaded region) of trajectory errors across test sequences. **e**, Velocity field distribution analysis using Kernel Density Estimation at  $t = 25$  s in the test set. The solid blue line represents the ground truth, the dashed red line denotes the predictions by TrajectoryFlowNet. **f**, Error distribution analysis of velocity predictions via Kernel Density Estimation at  $t = 25$  s in the test set.

velocities. This is most evident in the high-density regions ( $0.04 < \text{velocity} < 0.16$ ), where the reconstruction error in velocity distributions falls below the resolvability threshold. Visualizations of the predicted particle trajectories, velocity fields, and pressure fields are available in Supplementary Note. Notably, without imposing strong boundary condition constraints and solely relying on data-driven learning, the network was able to extract boundary features and effectively track particle trajectories and predict flow states in the irregular, unconfined boundary scenario.

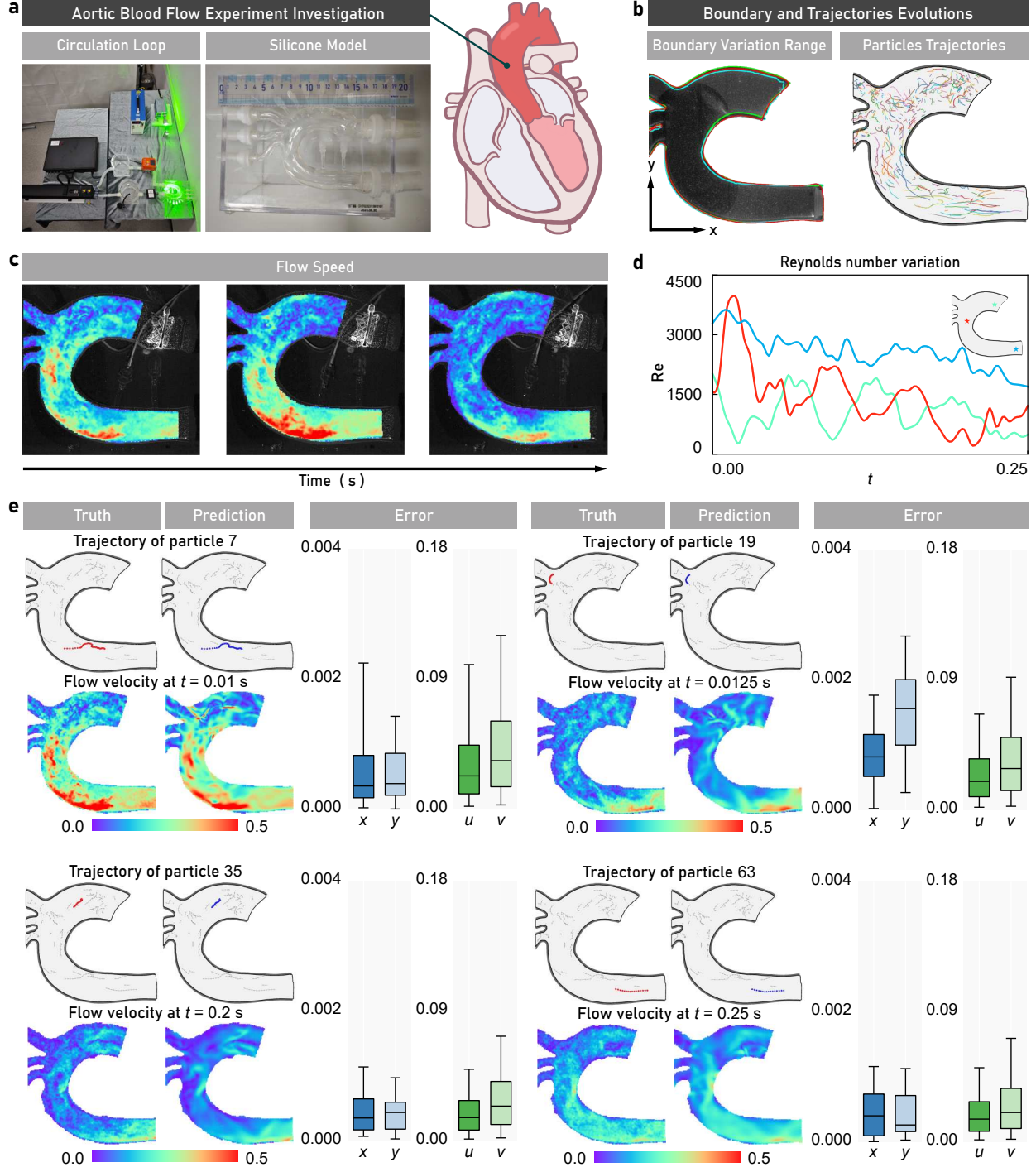


**Figure 4: Establishment of Aortic Blood Flow Case and Prediction Results.** a, The Aortic Blood Flow Experiment Investigation. b, The boundary and trajectory evolutions. c, Velocity field of the aortic blood flow obtained using the PIV method. d, Reynolds numbers measured upstream, downstream, and in the middle of the aorta, with line colors corresponding to position colors. e, Prediction results for the aortic blood flow case.

## Experimental aortic blood flow

Despite obtaining satisfactory data from the aforementioned results, TrajectoryFlowNet was only tested on idealized numerical simulation problems. However, for real-world problems, uncertainties

caused by measurement noise, varying boundary conditions, and source conditions pose significant challenges to data-driven modeling. For instance, the hemodynamic characteristics within the aorta are expected to be influenced by aortic displacement due to the periodic beating of the heart and its dynamic changes during systole. Given this, to apply TrajectoryFlowNet practically, we intentionally considered a real-world problem in the biomedical field, namely, predicting the flow dynamics in the aorta following balloon-expandable transcatheter aortic valve replacement (TAVR) (see Fig. 4a).

The dataset was established using laboratory data based on a silicone model of the aorta 3D printed from CT scans of healthy individuals. This model was then submerged in a working fluid composed of 62% water and 38% glycerol by volume, with 229.22 g/L urea added by weight to match the refractive index [75]. A 23 mm Edwards SAPIEN TAV was deployed at the annular position of the aortic root model. During systole, the blood-mimicking fluid flowed from the left ventricular compliance chamber through the TAV towards the aortic root, and then back to the left ventricle via resistance valves, a fluid reservoir, and a mitral valve. Time-resolved two-dimensional PIV experiments were conducted to measure the flow downstream of the TAV along the centerline of the root. An internal PIV software processed pairs of particle images, applying Gaussian filtering to reduce random noise, while also manually tracking particle trajectories. More details about this dataset can be found in Supplementary Note.

The inherent properties of real-world data such as intrinsic noise and missing information have an inherent impact on purely data-driven algorithms. Notably, the irregular moving boundaries of the aortic model present significant challenges for traditional methods aiming to establish physical models that replicate realistic conditions. Fig. 4b shows the range of variation in these model boundaries. Describing these boundary movements using neural networks based on regular grids is also challenging.

We used the trained TrajectoryFlowNet model to predict aortic flow field information over 50 time steps (0.25 seconds). Fig. 4a-d illustrate the predicted particle trajectories and velocity fields on the test set, with the box plots illustrate the distribution of normalized prediction errors for particle numbers and flow field time steps in the test dataset. The central box spans the interquartile range (25th–75th percentiles), the median marked by a horizontal line within the box. Lines extending from the box denote the 5th–95th percentile range. Clearly, our model effectively captures the evolving flow patterns following TAVR. Even in the presence of unknown uncertainties, correlation values for passive particle trajectories and velocities consistently exceeded 0.9, indicating accurate predictions. Without imposing explicit boundary conditions, our model demonstrates the capability to handle irregular moving boundaries. However, the real-world dataset considered in this example contains numerous elusive variables not present in our training data, which consists solely of displacement and velocity variables. Consequently, this limitation hinders accurate local predictions and reduces the performance of TrajectoryFlowNet.

## Experimental left ventricle blood flow

To further validate TrajectoryFlowNet’s capability for long-term particle trajectory tracking and flow field inversion even with limited data, we conducted an analysis of the flow dynamics within the left ventricle (LV) under physiological mitral valve conditions. This investigation is particularly significant given the challenges posed by inherent noise and missing data in real-world scenarios.

The dataset was established using laboratory data. The aortic root, aortic valve, and the complete mitral valve complex, including the annulus, anterior/posterior leaflets, chordae tendineae, and papillary muscles, were surgically dissected and sutured onto a 3D-printed annular resin plate connected to a silicone LV. The geometry of the silicone LV was reconstructed from adult heart

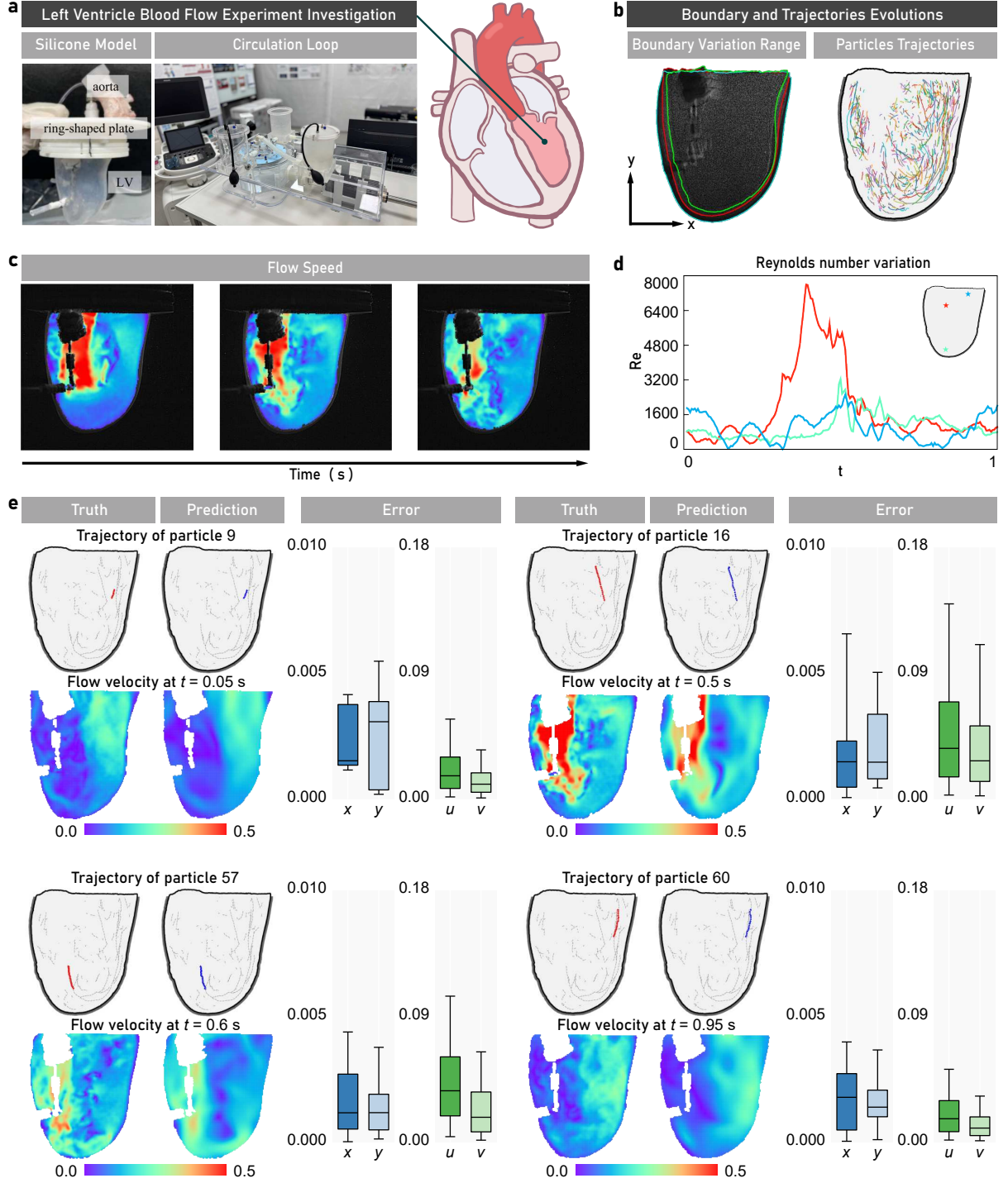


**Figure 5: Establishment of Left Ventricle Blood Flow Case and Prediction Results.** a, The Left Ventricle Blood Flow Experiment Investigation. b, The boundary and trajectory evolutions. c, Velocity field of the left ventricle blood flow obtained using the PIV method. d, Reynolds numbers measured upstream, downstream, and in the middle of the left ventricle, with line colors corresponding to position colors. e, Prediction results for the left ventricle blood flow case.

CT data, with a wall thickness of 2 mm and a refractive index of 1.4. The mitral valve-silicone LV



assembly was placed in a nonagonal chamber filled with a glycerol-water solution (62% water, 38% glycerol by volume), which had a dynamic viscosity of  $3.49\text{mPa} \cdot \text{s}$  at a temperature of  $26.9^\circ\text{C}$ . A piston driven by an electric motor generated periodic compression and relaxation of the chamber fluid to simulate LV systole and diastole, at a heart rate of 60 beats per minute and a cardiac output of 3.6 liters per minute. Time-resolved two-dimensional (2D) PIV experiments were conducted to track the flow states. Particle image pairs were processed using internal PIV software, while also manually tracking particle trajectories (see Fig. 5b). Further details about this dataset can be found in Supplementary Note.

Notably, our total training dataset comprised only 18,244 data points, averaging less than 92 data points per time step. Despite this, after training for just 1,000 epochs, TrajectoryFlowNet demonstrated remarkable performance. We applied the trained model to predict LV flow field information over 200 time steps (1 second). For the test set predictions, Fig. 5e displays both particle trajectories and velocity fields. The distribution of normalized prediction errors (for particle numbers and flow field time steps) across the test dataset is quantified via box plots. These plots show the interquartile range (25th–75th percentiles) as a box (median indicated by an internal line) and lines spanning the 5th–95th percentile range. Even without explicitly imposing boundary conditions, our model effectively captured long-term particle trajectories and evolving flow patterns within the LV. Correlation values for passive particle trajectories and velocities consistently exceeded 0.9, underscoring TrajectoryFlowNet’s proficiency in long-term predictions and flow field inversion with minimal data. These results highlight TrajectoryFlowNet’s robustness and efficiency in handling sparse datasets, making it a promising tool for biomedical applications such as cardiovascular imaging and disease screening.

## Discussion

This paper presents TrajectoryFlowNet, a deep learning model grounded in the Lagrangian Navier-Stokes equations, designed to predict particle trajectories and flow evolution. The model aims to forecast the movement of particles in a flow field based solely on their initial positions, while also estimating the flow field’s velocity and pressure. We developed a unique network architecture that integrates both Lagrangian and Eulerian perspectives, allowing for separate evaluations of passive particles. By incorporating the continuity equation and the Navier-Stokes equations, we introduce an inductive bias that alleviates the need for extensive training data. The ability of the neural network to learn high-frequency features was enhanced by employing Fourier feature mapping. As a result, the neural network exhibits strong interpretability and can generalize to predict trajectories of passive particles released from various initial positions and times, as well as the flow state at any spatial point.

We assessed the performance of TrajectoryFlowNet using both synthetic and field observation datasets across diverse flow scenarios, including Lid-Driven Cavity Flow, Complex Cylinder Flow, Experimental Aortic Blood Flow and Experimental left ventricle blood flow. Despite limited training data, the model effectively identifies dynamic patterns and demonstrates significant accuracy. The findings indicate that the trained model can predict flow states from any particle release position. In the Complex Cylinder Flow, TrajectoryFlowNet accurately captured the external boundaries without stringent boundary condition constraints, showcasing remarkable generalization capabilities. Additionally, the framework can reliably reveal and predict complex flow states around Experimental cases under uncertain conditions, even with limited real-world data. Overall, TrajectoryFlowNet is well-suited for learning predictions of randomly tracked particles in spatial domains of various geometries.

While TrajectoryFlowNet has shown its effectiveness and potential, it faces several challenges that require future attention. First, the fully connected layers within the model may encounter computational bottlenecks. We plan to address this by developing more efficient nonlinear training algorithms. Second, the model currently lacks the ability to quantify uncertainty in predictions when handling noisy real-world measurement data. Furthermore, its reliance on the distribution of passive particles in the flow field limits its predictive capabilities in areas with stagnant flow. Our future efforts will focus on implementing a training strategy with soft boundary constraints to mitigate uncertainty in flow states. Lastly, the model has only been applied to classical fluid dynamics problems, such as cylinder flow, and its ability to predict complex flow scenarios, including high Reynolds numbers and thermal flow coupling, remains to be explored.

## Methods

In this section, we introduce the proposed TrajectoryFlowNet model for tracking passive particle trajectories and flow field prediction. Additional details will be provided in Supplementary Note.

### Network architecture

We propose a novel TrajectoryFlowNet paradigm to simultaneously track particle trajectories and infer the flow field state. The innovative algorithm architecture is illustrated in Fig. 1, in which the network consists of Trajectory block and Flow Field block. Specifically, we leverage the flexibility of data-driven learning to integrate both Lagrangian and Eulerian descriptions within a unified model, thereby enhancing practical applicability in real-world scenarios.

Trajectory block aims to forecast the future movement paths of particles given only their initial positions. The latent solution  $\mathbf{x}$  is represented by the fully connected network  $\mathcal{N}_1$  as  $\mathbf{x}^\theta = \mathbf{x}(\mathbf{x}_0, t_0, \tau; \theta)$ . Here,  $\theta$  denotes the trainable parameters of  $\mathcal{N}_1$ . To further enhance the neural network’s ability to learn high-frequency features, we applied Fourier feature mapping  $\gamma_1$  to the spatiotemporal initial coordinates of particles and the Lagrangian description of motion time  $\gamma_1 = \gamma_1(\mathbf{x}_0, t_0, \tau; \mathbf{B}_1)$ . The network then takes these Fourier-matched inputs through multiple fully connected feedforward hidden layers (each with 40 nodes). We utilize hyperbolic tangent as a general activation function, known for its advantages in unbiased estimation of higher-order differentials and handling both positive and negative values. The subsequent output is based on linear activation through a generalized amplitude mapping.

Flow Field block considers the passive transport of particles, where the velocity of passive particles can be represented by the velocity of the flow field at their location. Predicting flow velocity and pressure entails estimating the velocity and pressure at a given position and time, based on known particle locations. The latent solution  $\{\mathbf{u}, p\}$  is interpreted by the fully connected network  $\mathcal{N}_2$  as  $\mathbf{u}^\vartheta = \mathbf{u}(\mathbf{x}, t; \vartheta)$ , where  $\vartheta$  represents the trainable parameters of  $\mathcal{N}_2$ . To facilitate the deduction of field characteristics, we apply Fourier feature matching using a Gaussian random matrix  $\mathbf{B}_2$  to the Eulerian spatiotemporal coordinates of particles  $\gamma_2 = \gamma_2(\mathbf{x}, t; \mathbf{B}_2)$ . The network  $\mathcal{N}_2$  then takes these Fourier-matched inputs through multiple fully connected feedforward hidden layers (each with 60 nodes), followed by using the hyperbolic tangent as the activation function.

TrajectoryFlowNet distinguishes between the two descriptions by inputting distinct temporal features of particle motion. This strategy ensures rigor in physical processes, particularly in partial differential equations, and enhances the network’s convergence capability. The model connects to physical laws through automatic differentiation, where trajectories predicted by fully connected network  $\mathcal{N}_1$  must align with the derivative of motion time in the Lagrangian description and correspond to the flow velocity predicted by fully connected network  $\mathcal{N}_2$  in the Eulerian spatiotemporal



domain, i.e.,  $\frac{d\mathbf{x}}{d\tau} = \mathbf{u}$ . Incorporating this physical information effectively balances the convergence consistency of both neural networks. Additionally, the flow velocity and pressure predicted by  $\mathcal{N}_2$  must satisfy the Navier-Stokes equations. All physical information is evaluated at machine precision at coordinate points.

## Motivation of the network architecture design

In previous sections, we introduced the proposed network architecture for tracking particle trajectories and inferring flow fields. Here, we elaborate on the design rationale to highlight key motivations. A distinguishing feature of our architecture is the integration of Lagrangian-Eulerian hybrid descriptions within a data-driven framework, enabling simultaneous tracking of particle motion and field characteristics. This contrasts with traditional numerical methods that rely on grid-based discretization and single-description frameworks, which suffer from strong coupling between particle counts and computational resources—particularly in unstructured grids where efficiency degrades significantly. Pure data-driven approaches, while avoiding explicit physical modeling, face challenges such as poor interpretability of black-box models, incompatibility with physical laws, and reliance on scarce training data.

To address these limitations, we innovatively developed a neural network with two blocks: Trajectory block, learns the spatiotemporal evolution of particle trajectories under the Lagrangian framework; Flow Field block, operating in the Eulerian framework, predicts the global velocity-pressure field. Physical constraints, including the Navier-Stokes equations and velocity consistency conditions, are embedded into the loss function via automatic differentiation, ensuring strict adherence to governing physics. This design transcends the limitations of single-description methods, enabling solutions to real-world problems. Compared to traditional physics-informed neural networks, our architecture exhibits stronger physical coupling: derivatives from Trajectory block are directly fed into Flow Field block, forming a closed-loop physical validation system. In contrast, PINN typically impose governing equations as soft constraints without bidirectional interaction.

The TrajectoryFlowNet architecture enables trajectory prediction and flow field inversion using only initial particle positions, thanks to its physics-aligned design. By employing MLP to model system states, the architecture inherently handles unstructured data, such as irregular boundaries and flow fields with embedded obstacles. Notably, it infers moving boundary information from sparse trajectory data without requiring explicit boundary condition inputs. To enhance capture of high-frequency features, Fourier feature mapping is applied, projecting input coordinates into a high-dimensional spectral space. This mitigates the spectral bias of neural networks, improving accuracy in regions with rapid spatial variations.

## Theoretical framework of TrajectoryFlowNet

The proposed TrajectoryFlowNet establishes a unified cross-description theoretical system through neural network parametrization of particle motion and flow field evolution, creating a dynamic coupling mechanism between Lagrangian and Eulerian descriptions to address limitations of traditional numerical methods in complex flow simulations. To substantiate these claims, we present the following theorems and lemmas demonstrating the effectiveness of our neural-based Lagrangian-Eulerian coupled dynamics framework.

**Lemma 1** (Lagrangian-Eulerian Equivalence). *Let the Lagrangian trajectory of a fluid parcel in continuum mechanics be described by the spatiotemporal mapping  $\mathbf{x}(\boldsymbol{\xi}, \tau) \in \mathbb{R}^d$ , whose dynamical*

evolution satisfies the initial value problem:

$$\frac{d\mathbf{x}}{d\tau} = \mathbf{u}(\mathbf{x}(\boldsymbol{\xi}, \tau), t), \quad \mathbf{x}(\boldsymbol{\xi}, 0) = \boldsymbol{\xi}, \quad (7)$$

where  $t = t_0 + \tau$  represents Eulerian time coordinates, and  $\mathbf{u} : \mathbb{R}^d \times \mathbb{R}^+ \rightarrow \mathbb{R}^d$  denotes the Eulerian velocity field. The material acceleration in Lagrangian framework maintains equivalence with the Eulerian material derivative:

$$\frac{d^2\mathbf{x}}{d\tau^2} \equiv \frac{D\mathbf{u}}{Dt} = \frac{\partial\mathbf{u}}{\partial t} + (\mathbf{u} \cdot \nabla_{\mathbf{x}})\mathbf{u}. \quad (8)$$

*Proof.* Applying the chain rule to Eq. (7), the Lagrangian acceleration expands as:

$$\frac{d^2\mathbf{x}}{d\tau^2} = \frac{d}{d\tau} \left( \frac{d\mathbf{x}}{d\tau} \right) = \frac{d\mathbf{u}(\mathbf{x}(\boldsymbol{\xi}, \tau), t)}{d\tau} = \frac{\partial\mathbf{u}}{\partial t} \cdot \frac{dt}{d\tau} + \nabla_{\mathbf{x}}\mathbf{u} \cdot \frac{d\mathbf{x}}{d\tau}. \quad (9)$$

Substituting  $\frac{dt}{d\tau} = 1$  and  $\frac{d\mathbf{x}}{d\tau} = \mathbf{u}$  completes the proof Eq. (8).  $\square$

**Theorem 1** (Neural Parametrization of Lagrangian Trajectories). *Define the trajectory learning network  $\mathcal{N}_1(\boldsymbol{\theta}) : \mathbb{R}^d \times \mathbb{R}^+ \times \mathbb{R}^+ \rightarrow \mathbb{R}^d$  with inputs: initial position  $\mathbf{x}_0 \in \Omega$ , release time  $t_0 \in [0, T]$ , and Lagrangian time  $\tau \in [0, \Delta T]$ . The complete trajectory is parametrized as:*

$$\mathbf{x}_{\boldsymbol{\theta}}(\tau) = \mathbf{x}_0 + \tilde{\mathbf{x}}_{\boldsymbol{\theta}}(\mathbf{x}_0, t_0, \tau). \quad (10)$$

Using  $C^2$ -continuous activation functions (e.g., Tanh) in  $\mathcal{N}_1$ , the predicted Lagrangian velocity field  $\mathbf{u}_{\boldsymbol{\theta}} = \partial\mathbf{x}_{\boldsymbol{\theta}}/\partial\tau$  satisfies differential compatibility:

$$\mathbf{u}_{\boldsymbol{\theta}} = \frac{\partial\tilde{\mathbf{x}}_{\boldsymbol{\theta}}}{\partial\tau}, \quad \frac{\partial\mathbf{u}_{\boldsymbol{\theta}}}{\partial\tau} = \frac{\partial^2\tilde{\mathbf{x}}_{\boldsymbol{\theta}}}{\partial\tau^2}. \quad (11)$$

*Proof.* The use of sufficiently smooth activation functions in the neural network enables accurate computation of higher-order derivatives through automatic differentiation. The displacement increment parametrization in Eq. (10) ensures explicit correlation between velocity and displacement fields, while the deterministic mapping property preserves spatiotemporal continuity.  $\square$

**Lemma 2** (Velocity Consistency Constraint). *Let the Eulerian velocity field be modeled by network  $\mathcal{N}_2(\boldsymbol{\vartheta}) : \mathbb{R}^d \times \mathbb{R}^+ \rightarrow \mathbb{R}^d \times \mathbb{R}$ , which outputs velocity-pressure pairs  $(\mathbf{u}_{\boldsymbol{\vartheta}}, p_{\boldsymbol{\vartheta}})$ . If  $\mathcal{N}_1$  satisfies the kinematic equation (7), then the Lagrangian and Eulerian velocity fields must satisfy the following strong consistency condition:*

$$\mathbf{u}_{\boldsymbol{\vartheta}}(\mathbf{x}_{\boldsymbol{\theta}}(\tau), t_0 + \tau) = \mathbf{u}_{\boldsymbol{\theta}}(\mathbf{x}_0, t_0, \tau), \quad \forall \tau \in [0, \Delta T]. \quad (12)$$

*Proof.* By trajectory parametrization,  $\mathbf{x}_{\boldsymbol{\theta}}(\tau)$  implicitly encodes passive particle motion history. When this trajectory is substituted into the Eulerian frame, the velocity of the particle must coincide with the local Eulerian velocity field evaluated along the path. Specifically, since the Lagrangian velocity is defined as  $\mathbf{u}_{\boldsymbol{\theta}} = d\mathbf{x}_{\boldsymbol{\theta}}/d\tau$ , the consistency condition arises naturally from the equivalence between material derivative and local measurement in the Eulerian framework.  $\square$

**Theorem 2** (Navier-Stokes Residual Constraint). *If the neural network  $\mathcal{N}_2$  predicts a velocity-pressure pair  $(\mathbf{u}_{\boldsymbol{\vartheta}}, p_{\boldsymbol{\vartheta}})$  that satisfies the incompressible Navier-Stokes equations:*

$$\frac{\partial\mathbf{u}_{\boldsymbol{\vartheta}}}{\partial t} + (\mathbf{u}_{\boldsymbol{\vartheta}} \cdot \nabla)\mathbf{u}_{\boldsymbol{\vartheta}} = -\frac{1}{\rho}\nabla p_{\boldsymbol{\vartheta}} + \nu\nabla^2\mathbf{u}_{\boldsymbol{\vartheta}}, \quad \nabla \cdot \mathbf{u}_{\boldsymbol{\vartheta}} = 0, \quad (13)$$

then the trajectory network  $\mathcal{N}_1$  must obey the following dynamic constraint relating its second-order temporal derivative to the material derivative of the Eulerian velocity field:

$$\frac{d^2 \mathbf{x}_\theta}{d\tau^2} = \frac{D\mathbf{u}_\theta}{Dt} \Big|_{\mathbf{x}=\mathbf{x}_\theta(\tau), t=t_0+\tau}, \quad (14)$$

where  $D/Dt = \partial_t + \mathbf{u}_\theta \cdot \nabla$  denotes the material derivative.

*Proof.* From Lemma 1, we have the identity:

$$\frac{d^2 \mathbf{x}_\theta}{d\tau^2} = \frac{d}{d\tau} \mathbf{u}_\theta. \quad (15)$$

By Lemma 2, the Lagrangian velocity  $\mathbf{u}_\theta$  is equal to the Eulerian velocity evaluated along the trajectory:

$$\mathbf{u}_\theta(\tau) = \mathbf{u}_\theta(\mathbf{x}_\theta(\tau), t_0 + \tau). \quad (16)$$

Taking the total time derivative on both sides, we obtain:

$$\frac{d}{d\tau} \mathbf{u}_\theta = \frac{D\mathbf{u}_\theta}{Dt} \Big|_{\mathbf{x}=\mathbf{x}_\theta(\tau), t=t_0+\tau}. \quad (17)$$

Therefore, combining these results gives:

$$\frac{d^2 \mathbf{x}_\theta}{d\tau^2} = \frac{D\mathbf{u}_\theta}{Dt} \Big|_{\mathbf{x}=\mathbf{x}_\theta(\tau), t=t_0+\tau}, \quad (18)$$

which completes the proof.  $\square$

The mathematical derivations in Theorem 1 and Lemma 2 ensure strong consistency between Lagrangian trajectory network  $\mathcal{N}_1$  and Eulerian field network  $\mathcal{N}_2$  at both velocity and acceleration levels (Eqs. (12) and (14)), overcoming physical distortion from coordinate decoupling in traditional methods. Theorem 2 enforces physical fidelity through Navier-Stokes residual constraints. The neural network architecture dynamically couples Lagrangian trajectory tracking with Eulerian field evolution while maintaining differential compatibility (Eq. (11)) via automatic differentiation. Embedded physical constraints guarantee solution plausibility through nonlinear function approximation.

## Loss function

The physics-constrained loss function consists of two components: the data loss  $L_d$  and the residual physics loss  $L_p$ . The data loss is defined as:

$$L_d(\boldsymbol{\theta}, \boldsymbol{\vartheta}) = \frac{1}{dN_m T} \|\hat{\mathbf{x}} - \mathbf{x}\|_2^2 + \frac{1}{dN_m T} \|\hat{\mathbf{u}} - \mathbf{u}\|_2^2, \quad (19)$$

which calculates the aggregated mean square errors (MSE) between the predicted data  $\hat{\mathbf{x}} \in \mathbb{R}^{d \times N_m \times T}$ ,  $\hat{\mathbf{u}} \in \mathbb{R}^{d \times N_m \times T}$  and the training labels  $\mathbf{x} \in \mathbb{R}^{d \times N_m \times T}$ ,  $\mathbf{u} \in \mathbb{R}^{d \times N_m \times T}$  to optimize the trainable parameters  $(\boldsymbol{\theta}, \boldsymbol{\vartheta})$  in our model. Here,  $d$  denotes the system dimension;  $N_m$  the total training number of particles;  $T$  the number of time steps in training and  $\|\cdot\|_2$  denotes the Frobenius norm.

The physics loss function is formulated as:

$$L_p(\boldsymbol{\theta}, \boldsymbol{\vartheta}) = \frac{1}{N_c} \left\| \left( \frac{d\hat{\mathbf{x}}}{d\tau} \right) - \hat{\mathbf{u}} \right\|_2^2 + \frac{1}{N_c} \left\| \left( \frac{d\hat{\mathbf{x}}}{dt} + (\hat{\mathbf{u}} \cdot \nabla) \hat{\mathbf{u}} + \frac{1}{\rho} \nabla \hat{p} + \frac{\hat{\mu}}{\rho} \nabla^2 \hat{\mathbf{u}} \right) \right\|_2^2, \quad (20)$$

where the predicted data  $\hat{\mathbf{x}} \in \mathbb{R}^{d \times N_c \times T}$ ,  $\hat{\mathbf{u}} \in \mathbb{R}^{d \times N_c \times T}$ ,  $\hat{p} \in \mathbb{R}^{N_c \times T}$  and  $\hat{\mu} \in \mathbb{R}^{N_c \times T}$  together constitute physical constraints (Eqs. 5 and 6) to optimize the trainable parameters  $(\boldsymbol{\theta}, \boldsymbol{\vartheta})$  in our model. Here,  $N_c$  denotes the total number of collocation particles.

## Normalization

In this study, we adopt a normalization approach inspired by traditional fluid mechanics methods, which involves dimensionless treatment of all physical quantities using minimal reference values. Specifically, we normalize spatial positions and velocities in the dataset by their respective maximum values  $L$  and  $U$ :

$$\mathbf{x}^* = \frac{\mathbf{x}}{L}, \quad \mathbf{u}^* = \frac{\mathbf{u}}{U}, \quad p^* = \frac{p}{\rho U^2}, \quad t^* = \frac{tU}{L}. \quad (21)$$

This normalization transforms the Navier-Stokes equations to:

$$\left( \frac{\partial \bar{\mathbf{u}}}{\partial \bar{t}} + (\bar{\mathbf{u}} \cdot \bar{\nabla}) \bar{\mathbf{u}} \right) = -\frac{\bar{P}}{\rho U^2} \bar{\nabla} \bar{p} + \frac{\mu}{\rho U L} \bar{\nabla}^2 \bar{\mathbf{v}}. \quad (22)$$

Applying this method confines data ranges to the  $[-1, 1]$  interval, complementing the use of the hyperbolic tangent ( $\tanh$ ) activation function to expedite convergence during the training phase.

## Fourier feature mapping

Fourier feature mapping transforms input points to the surface of a higher-dimensional hypersphere using a set of sinusoids, enabling neural networks to learn high-frequency functions in low-dimensional problems. Specifically, this involves converting the Neural Tangent Kernel (NTK) into a stationary kernel by modifying the frequency vectors  $b_j$  to adjust the NTK's spectrum, thereby controlling the learning range of the neural network. We applied random Gaussian feature mapping before each input to the neural network:

$$\gamma(\mathbf{v}) = [\cos(2\pi \mathbf{B}\mathbf{v}), \sin(2\pi \mathbf{B}\mathbf{v})]^T. \quad (23)$$

The matrix  $\mathbf{B}$  is randomly generated with Gaussian elements  $B_{ij} \sim \mathcal{N}(0, \sigma^2)$ , where  $\sigma$  is a hyperparameter tuned according to different tasks. Specific parameter choices are detailed in the supplementary files.

## Experimental setup and computational resources

All models were trained using the L-BFGS optimizer with a learning rate of 1.0. The optimization process involved a maximum of 50,000 iterations and computations per optimization function. For the Lid-Driven Cavity Flow case, Trajectory block used a 4-layer MLP with 40 neurons per hidden layer, while Flow Field block used a 6-layer MLP with 60 neurons per layer. For Complex Cylinder Flow, Trajectory block's architecture was updated to 10 hidden layers, keeping other parameters constant. For Experimental Aortic Blood Flow, Flow Field block similarly adopted 10 hidden layers, with unchanged remaining settings. Training took place on a server equipped with an Intel(R) Xeon(R) Platinum 8380 CPU (2.30GHz, 64 cores) and NVIDIA A100 GPU (80GB).

## Data availability

All the used datasets in this study are available on GitHub at <https://xxxx>.

## Code availability

All the source codes to reproduce the results in this study are available on GitHub at <https://xxxx>.

## References

- [1] Matthew D. Grossi, Miroslav Kubat, and Tamay M. Özgökmen. Predicting particle trajectories in oceanic flows using artificial neural networks. *Ocean Modelling*, 156:101707, December 2020.
- [2] Alex Krizhevsky, Ilya Sutskever, and Geoffrey E. Hinton. Imagenet classification with deep convolutional neural networks. *Communications of the ACM*, 60(6):84–90, May 2017.
- [3] Thorsten Kurth, Sean Treichler, Joshua Romero, Mayur Mudigonda, Nathan Luehr, Everett Phillips, Ankur Mahesh, Michael Matheson, Jack Deslippe, Massimiliano Fatica, Prabhat, and Michael Houston. Exascale deep learning for climate analytics, October 2018.
- [4] A. C. Haza, N. Paldor, T. M. Özgökmen, M. Curcic, S. S. Chen, and G. Jacobs. Wind-based estimations of ocean surface currents from massive clusters of drifters in the gulf of mexico. *Journal of Geophysical Research: Oceans*, 124(8):5844–5869, August 2019.
- [5] Babak Alipanahi, Andrew Delong, Matthew T Weirauch, and Brendan J Frey. Predicting the sequence specificities of dna- and rna-binding proteins by deep learning. *Nature Biotechnology*, 33(8):831–838, August 2015.
- [6] B. M. Lake, R. Salakhutdinov, and J. B. Tenenbaum. Human-level concept learning through probabilistic program induction. *Science*, 350(6266):1332–1338, December 2015.
- [7] D. Sushma Reddy and P. Rama Chandra Prasad. Prediction of vegetation dynamics using ndvi time series data and lstm. *Modeling Earth Systems and Environment*, 4(1):409–419, April 2018.
- [8] Hugh Roarty, Scott Glenn, Josh Kohut, Donglai Gong, Ethan Handel, Erick Rivera, Teresa Garner, Larry Atkinson, Wendell Brown, Chris Jakubiak, Mike Muglia, Sara Haines, and Harvey Seim. Operation and application of a regional high-frequency radar network in the mid-atlantic bight. *Marine Technology Society Journal*, 44(6):133–145, November 2010.
- [9] Fred H. Sklar and Joan A. Browder. Coastal environmental impacts brought about by alterations to freshwater flow in the gulf of mexico. *Environmental Management*, 22(4):547–562, July 1998.
- [10] Cecilia Enriquez, Ismael J Mariño-Tapia, and Jorge A Herrera-Silveira. Dispersion in the yucatan coastal zone: Implications for red tide events. *Continental Shelf Research*, 30(2):127–137, February 2010.
- [11] M. Raissi, P. Perdikaris, and G.E. Karniadakis. Physics-informed neural networks: A deep learning framework for solving forward and inverse problems involving nonlinear partial differential equations. *Journal of Computational Physics*, 378:686–707, February 2019.
- [12] Atilim Gunes Baydin, Barak A Pearlmutter, Alexey Andreyevich Radul, and Jeffrey Mark Siskind. Automatic differentiation in machine learning: a survey. *Journal of machine learning research*, 18(153):1–43, 2018.
- [13] Jiun-Shyan Chen, Michael Hillman, and Sheng-Wei Chi. Meshfree methods: Progress made after 20 years. *Journal of Engineering Mechanics*, 143(4):04017001, 2017.
- [14] George Em Karniadakis, Ioannis G. Kevrekidis, Lu Lu, Paris Perdikaris, Sifan Wang, and Liu Yang. Physics-informed machine learning. *Nature Reviews Physics*, 3(6):422–440, 2021.

- [15] Xiaowei Jin, Shengze Cai, Hui Li, and George Em Karniadakis. Nsfnets (navier-stokes flow nets): Physics-informed neural networks for the incompressible navier-stokes equations. *Journal of Computational Physics*, 426:109951, 2021.
- [16] Zhenhua Xia, Yipeng Shi, Qingqing Zhang, and Shiyi Chen. Modulation to compressible homogenous turbulence by heavy point particles. i. effect of particles' density. *Physics of Fluids*, 28(1):016103, January 2016.
- [17] Yantao Yang, Jianchun Wang, Yipeng Shi, Zuoli Xiao, X. T. He, and Shiyi Chen. Interactions between inertial particles and shocklets in compressible turbulent flow. *Physics of Fluids*, 26(9):091702, September 2014.
- [18] Federico Toschi and Eberhard Bodenschatz. Lagrangian properties of particles in turbulence. *Annual Review of Fluid Mechanics*, 41(1):375–404, January 2009.
- [19] Markus Uhlmann. Interface-resolved direct numerical simulation of vertical particulate channel flow in the turbulent regime. *Physics of Fluids*, 20(5):053305, May 2008.
- [20] P. Bagchi and S. Balachandar. Effect of turbulence on the drag and lift of a particle. *Physics of Fluids*, 15(11):3496–3513, November 2003.
- [21] J. G. M. Kuerten. Point-particle dns and les of particle-laden turbulent flow - a state-of-the-art review. *Flow, Turbulence and Combustion*, 97(3):689–713, October 2016.
- [22] S. Balachandar and John K. Eaton. Turbulent dispersed multiphase flow. *Annual Review of Fluid Mechanics*, 42(1):111–133, January 2010.
- [23] Allan Pinkus. Approximation theory of the mlp model in neural networks. *Acta Numerica*, 8:143–195, January 1999.
- [24] Huizan Wang, Ding Liu, Weimin Zhang, Jiaxun Li, and Bo Wang. Characterizing the capability of mesoscale eddies to carry drifters in the northwest pacific. *Journal of Oceanology and Limnology*, 38(6):1711–1728, November 2020.
- [25] Markus Raffel, editor. *Particle Image Velocimetry: A Practical Guide*. Springer, Heidelberg ; New York, 2nd ed edition, 2007.
- [26] Maziar Raissi, Alireza Yazdani, and George Em Karniadakis. Hidden fluid mechanics: Learning velocity and pressure fields from flow visualizations. *Science*, 367(6481):1026–1030, February 2020.
- [27] Paris Perdikaris, Daniele Venturi, and George Em Karniadakis. Multifidelity information fusion algorithms for high-dimensional systems and massive data sets. *SIAM Journal on Scientific Computing*, 38(4):B521–B538, January 2016.
- [28] Pijush K. Kundu, Ira M. Cohen, and Howard H. Hu. *Fluid Mechanics*. Elsevier Academic Press, Amsterdam ; Boston, 3rd ed edition, 2004.
- [29] Eberhard Grün, Mihaly Horanyi, and Zoltan Sternovsky. The lunar dust environment. *Planetary and Space Science*, 59(14):1672–1680, November 2011.
- [30] Thomas Bolton and Laure Zanna. Applications of deep learning to ocean data inference and subgrid parameterization. *Journal of Advances in Modeling Earth Systems*, 11(1):376–399, January 2019.



- [31] Mark W. Tibbitt, James E. Dahlman, and Robert Langer. Emerging frontiers in drug delivery. *Journal of the American Chemical Society*, 138(3):704–717, January 2016.
- [32] Adam A. Dmytriw, Jin Soo A. Song, Eugene Yu, and Colin S. Poon. Cerebral venous thrombosis: State of the art diagnosis and management. *Neuroradiology*, 60(7):669–685, July 2018.
- [33] Mark Alber, Adrian Buganza Tepole, William R. Cannon, Suvranu De, Salvador Dura-Bernal, Krishna Garikipati, George Karniadakis, William W. Lytton, Paris Perdikaris, Linda Petzold, and Ellen Kuhl. Integrating machine learning and multiscale modeling—perspectives, challenges, and opportunities in the biological, biomedical, and behavioral sciences. *npj Digital Medicine*, 2(1):115, November 2019.
- [34] Michael Durand, Lee-Lueng Fu, Dennis P. Lettenmaier, Douglas E. Alsdorf, Ernesto Rodriguez, and Daniel Esteban-Fernandez. The surface water and ocean topography mission: Observing terrestrial surface water and oceanic submesoscale eddies. *Proceedings of the IEEE*, 98(5):766–779, May 2010.
- [35] Victoria Futch and Arthur Allen. Search and rescue applications: On the need to improve ocean observing data systems in offshore or remote locations. *Frontiers in Marine Science*, 6:301, June 2019.
- [36] Henry Stommel. The westward intensification of wind-driven ocean currents. *Transactions, American Geophysical Union*, 29(2):202, 1948.
- [37] Tatsu Isaji, Malcolm L. Spaulding, and Arthur A. Allen. Stochastic particle trajectory modeling techniques for spill and search and rescue models. In *Estuarine and Coastal Modeling (2005)*, pages 537–547, Charleston, South Carolina, United States, July 2006. American Society of Civil Engineers.
- [38] Kurt Hornik, Maxwell Stinchcombe, and Halbert White. Multilayer feedforward networks are universal approximators. *Neural Networks*, 2(5):359–366, January 1989.
- [39] Kaichao You, Mingsheng Long, Jianmin Wang, and Michael I. Jordan. How does learning rate decay help modern neural networks?, September 2019.
- [40] P. Y. Le Traon, F. Nadal, and N. Ducet. An improved mapping method of multisatellite altimeter data. *Journal of Atmospheric and Oceanic Technology*, 15(2):522–534, April 1998.
- [41] Sung Yong Kim, Eric J. Terrill, and Bruce D. Cornuelle. Mapping surface currents from hf radar radial velocity measurements using optimal interpolation. *Journal of Geophysical Research: Oceans*, 113(C10):2007JC004244, October 2008.
- [42] Rick Lumpkin, Tamay Özgökmen, and Luca Centurioni. Advances in the application of surface drifters. *Annual Review of Marine Science*, 9(1):59–81, January 2017.
- [43] Maristella Berta, Annalisa Griffa, Marcello G. Magaldi, Tamay M. Özgökmen, Andrew C. Poje, Angelique C. Haza, and M. Josefina Olascoaga. Improved surface velocity and trajectory estimates in the gulf of mexico from blended satellite altimetry and drifter data. *Journal of Atmospheric and Oceanic Technology*, 32(10):1880–1901, October 2015.
- [44] Alexander H. Meier and Thomas Roesgen. Imaging laser doppler velocimetry. *Experiments in Fluids*, 52(4):1017–1026, April 2012.

- [45] Tamay Özgökmen, Eric Chassignet, Clint Dawson, Dmitry Dukhovskoy, Gregg Jacobs, James Ledwell, Oscar Garcia-Pineda, Ian MacDonald, Steven Morey, Maria Olascoaga, Andrew Poje, Mark Reed, and Jorgen Skancke. Over what area did the oil and gas spread during the 2010 deepwater horizon oil spill? *Oceanography*, 29(3):96–107, September 2016.
- [46] Andrew C. Poje, Tamay M. Özgökmen, Bruce L. Lipphardt, Brian K. Haus, Edward H. Ryan, Angelique C. Haza, Gregg A. Jacobs, A. J. H. M. Reniers, Maria Josefine Olascoaga, Guillaume Novelli, Annalisa Griffa, Francisco J. Beron-Vera, Shuyi S. Chen, Emanuel Coelho, Patrick J. Hogan, Albert D. Kirwan, Helga S. Huntley, and Arthur J. Mariano. Submesoscale dispersion in the vicinity of the *deepwater horizon* spill. *Proceedings of the National Academy of Sciences*, 111(35):12693–12698, September 2014.
- [47] Maziar Raissi, Zhicheng Wang, Michael S. Triantafyllou, and George Em Karniadakis. Deep learning of vortex induced vibrations. *Journal of Fluid Mechanics*, 861:119–137, February 2019.
- [48] François Gheusi and Joël Stein. Lagrangian description of airflows using eulerian passive tracers. *Quarterly Journal of the Royal Meteorological Society: A journal of the atmospheric sciences, applied meteorology and physical oceanography*, 128(579):337–360, 2002.
- [49] Douglas H. Kelley, Michael R. Allshouse, and Nicholas T. Ouellette. Lagrangian coherent structures separate dynamically distinct regions in fluid flows. *Physical Review E*, 88(1):013017, July 2013.
- [50] Guilherme S. Vieira and Michael R. Allshouse. Internal wave boluses as coherent structures in a continuously stratified fluid. *Journal of Fluid Mechanics*, 885:A35, February 2020. arXiv:1907.10103 [physics].
- [51] Stefania Espa and Giorgio Querzoli. Lagrangian Analysis of passive tracers dispersion in a confined convective flow.
- [52] Guilherme S. Vieira, Michael R. Allshouse, and Amala Mahadevan. Seagrass deformation affects fluid instability and tracer exchange in canopy flow. *Scientific Reports*, 13(1):3910, March 2023.
- [53] Leonid Kuznetsov and George M Zaslavsky. Passive particle transport in three-vortex flow. *Physical Review E*, 61(4):3777, 2000.
- [54] PD Miller, CKRT Jones, AM Rogerson, and LJ Pratt. Quantifying transport in numerically generated velocity fields. *Physica D: Nonlinear Phenomena*, 110(1-2):105–122, 1997.
- [55] George Haller and AC Poje. Finite time transport in aperiodic flows. *Physica D: Nonlinear Phenomena*, 119(3-4):352–380, 1998.
- [56] Andrea Crisanti, Massimo Falcioni, Antonello Provenzale, Paolo Tanga, and Angelo Vulpiani. Dynamics of passively advected impurities in simple two-dimensional flow models. *Physics of Fluids A: Fluid Dynamics*, 4(8):1805–1820, 1992.
- [57] Andrea Crisanti, Massimo Falcioni, Angelo Vulpiani, and Giovanni Paladin. Lagrangian chaos: transport, mixing and diffusion in fluids. *La Rivista del Nuovo Cimento (1978-1999)*, 14:1–80, 1991.
- [58] V Rom-Kedar, A Leonard, and S Wiggins. An analytical study of transport, mixing and chaos in an unsteady vortical flow. *Journal of Fluid Mechanics*, 214:347–394, 1990.

- [59] Julio M Ottino et al. Mixing, chaotic advection, and turbulence. *Annual Review of Fluid Mechanics*, 22(1):207–254, 1990.
- [60] Julio M Ottino. *The kinematics of mixing: stretching, chaos, and transport*, volume 3. Cambridge university press, 1989.
- [61] Hassan Aref. Chaotic advection of fluid particles. *Philosophical Transactions of the Royal Society of London. Series A: Physical and Engineering Sciences*, 333(1631):273–288, 1990.
- [62] Elizabeth A Andruszkiewicz, Jeffrey R Koseff, Oliver B Fringer, Nicholas T Ouellette, Anna B Lowe, Christopher A Edwards, and Alexandria B Boehm. Modeling environmental dna transport in the coastal ocean using lagrangian particle tracking. *Frontiers in Marine Science*, 6:477, 2019.
- [63] Oveis Pourmehran, Mohammad Rahimi-Gorji, M Gorji-Bandpy, and TB Gorji. Simulation of magnetic drug targeting through tracheobronchial airways in the presence of an external non-uniform magnetic field using lagrangian magnetic particle tracking. *Journal of Magnetism and Magnetic Materials*, 393:380–393, 2015.
- [64] Oveis Pourmehran, Tahereh B Gorji, and Mofid Gorji-Bandpy. Magnetic drug targeting through a realistic model of human tracheobronchial airways using computational fluid and particle dynamics. *Biomechanics and modeling in mechanobiology*, 15(5):1355–1374, 2016.
- [65] Erik Van Sebille, Stephen M Griffies, Ryan Abernathey, Thomas P Adams, Pavel Berloff, Arne Biastoch, Bruno Blanke, Eric P Chassignet, Yu Cheng, Colin J Cotter, et al. Lagrangian ocean analysis: Fundamentals and practices. *Ocean modelling*, 121:49–75, 2018.
- [66] Jinhua Wang, Yongming Shen, and Yakun Guo. Seasonal circulation and influence factors of the bohai sea: a numerical study based on lagrangian particle tracking method. *Ocean dynamics*, 60:1581–1596, 2010.
- [67] Simon Unterstrasser and Ingo Sölch. Study of contrail microphysics in the vortex phase with a lagrangian particle tracking model. *Atmospheric Chemistry and Physics*, 10(20):10003–10015, 2010.
- [68] John Lin, Dominik Brunner, Christoph Gerbig, Andreas Stohl, Ashok Luhar, and Peter Webley. *Lagrangian modeling of the atmosphere*. John Wiley & Sons, 2013.
- [69] Ronald J Adrian. Twenty years of particle image velocimetry. *Experiments in fluids*, 39:159–169, 2005.
- [70] Jerry Westerweel, Gerrit E Elsinga, and Ronald J Adrian. Particle image velocimetry for complex and turbulent flows. *Annual Review of Fluid Mechanics*, 45(1):409–436, 2013.
- [71] Ian Grant. Particle image velocimetry: a review. *Proceedings of the Institution of Mechanical Engineers, Part C: Journal of Mechanical Engineering Science*, 211(1):55–76, 1997.
- [72] Lucas C Laurindo, Arthur J Mariano, and Rick Lumpkin. An improved near-surface velocity climatology for the global ocean from drifter observations. *Deep Sea Research Part I: Oceanographic Research Papers*, 124:73–92, 2017.
- [73] Salvatore Cuomo, Vincenzo Schiano Di Cola, Fabio Giampaolo, Gianluigi Rozza, Maziar Raissi, and Francesco Piccialli. Scientific machine learning through physics-informed neural networks: Where we are and what’s next. *Journal of Scientific Computing*, 92(3):88, 2022.

- [74] Shengze Cai, Zhiping Mao, Zhicheng Wang, Minglang Yin, and George Em Karniadakis. Physics-informed neural networks (pinns) for fluid mechanics: A review. *Acta Mechanica Sinica*, 37(12):1727–1738, 2021.
- [75] Huang Chen and Lakshmi Prasad Dasi. An in-vitro study of the flow past a transcatheter aortic valve using time-resolved 3d particle tracking. *Annals of Biomedical Engineering*, 51(7):1449–1460, 2023.
- [76] Mohammad Habeeb, Hariharan Thirumalai Vengateswaran, Arpan Kumar Tripathi, Smita Tukaram Kumbhar, Huay Woon You, et al. Enhancing biomedical imaging: the role of nanoparticle-based contrast agents. *Biomedical Microdevices*, 26(4):1–18, 2024.
- [77] Marketa Ryvolova, Jana Chomoucka, Jana Drbohlavova, Pavel Kopel, Petr Babula, David Hynek, Vojtech Adam, Tomas Eckschlager, Jaromir Hubalek, Marie Stiborova, et al. Modern micro and nanoparticle-based imaging techniques. *Sensors*, 12(11):14792–14820, 2012.
- [78] Maziar Raissi, Alireza Yazdani, and George Em Karniadakis. Hidden fluid mechanics: Learning velocity and pressure fields from flow visualizations. *Science*, 367(6481):1026–1030, 2020.
- [79] Zhao Chen, Yang Liu, and Hao Sun. Physics-informed learning of governing equations from scarce data. *Nature communications*, 12(1):6136, 2021.
- [80] Hongping Wang, Yi Liu, and Shizhao Wang. Dense velocity reconstruction from particle image velocimetry/particle tracking velocimetry using a physics-informed neural network. *Physics of fluids*, 34(1), 2022.
- [81] Shengze Cai, He Li, Fuyin Zheng, Fang Kong, Ming Dao, George Em Karniadakis, and Subra Suresh. Artificial intelligence velocimetry and microaneurysm-on-a-chip for three-dimensional analysis of blood flow in physiology and disease. *Proceedings of the National Academy of Sciences*, 118(13):e2100697118, 2021.

## Acknowledgement

The work is supported by the Strategic Priority Research Program of the Chinese Academy of Sciences (No. XDB0620103) and the Fundamental Research Funds for the Central Universities (No. E2EG2202X2).

## Author contributions

J.W. and Y.L. contributed to the ideation and design of the research; J.W., H.W., B.L. and Y.L. performed the research; G.H. and Y.L. supervised the work; all authors contributed to writing and editing the paper.

## Corresponding authors

Yang Liu ([liuyang22@ucas.ac.cn](mailto:liuyang22@ucas.ac.cn)).

## **Competing interests**

The authors declare no competing interests.

## **Supplementary information:**

The supplementary information is attached.

# TrajectoryFlowNet: Hybrid Lagrangian–Eulerian learning of flow field and trajectories

Jingdi Wan<sup>1</sup>, Hongping Wang<sup>2</sup>, Bo Liu<sup>1</sup>, Guowei He<sup>1,2</sup>, Yang Liu<sup>1,2\*</sup>

<sup>1</sup>School of Engineering Science, University of Chinese Academy of Sciences, Beijing, China

<sup>2</sup>Institute of Mechanics, Chinese Academy of Sciences, Beijing, China

\*Corresponding authors

## Contents

<b>A Background</b>	<b>1</b>
<b>B Methodology</b>	<b>2</b>
B.1 Algorithm Description . . . . .	2
B.2 Variables Notation . . . . .	3
<b>C Dataset</b>	<b>3</b>
C.1 Lid-driven Cavity Flow . . . . .	4
C.2 Complex Cylinder Flow . . . . .	5
C.3 Experimental Aortic Blood Flow . . . . .	5
C.4 Experimental Left Ventricle Blood Flow . . . . .	6
<b>D Results</b>	<b>7</b>
D.1 Fourier feature mapping . . . . .	7
D.2 Impact of Physical Constraints . . . . .	8
D.3 Activation function . . . . .	8

This supplementary document provides a detailed description of the proposed TrajectoryFlowNet model, examples, and additional test results.

## A Background

The research on tracking and quantifying flow fields aims to investigate and elucidate the formation, instability, and predictive capabilities of complex flow states. Predicting the motion paths of passive particles within a flow, while simultaneously inferring the flow’s velocity and pressure, is crucial for addressing practical challenges in fields such as weather forecasting, combustion processes, and maritime search and rescue. The partial differential nature of the Navier-Stokes (NS) equations makes solving these problems particularly challenging. In recent years, machine learning has shown great promise in tackling fluid mechanics issues described by partial differential equations. In this paper, we focus on incorporating prior physical knowledge into artificial intelligence to learn the motion states of passive particles in flow fields and, based on this, reverse-engineer the temporal evolution of the flow. The following section provides basic information on the fully connected neural network used in this study.



**Fully Connected Neural Network.** A fully connected neural network (FCNN) [1] is a type of artificial neural network that is used for solving various machine learning tasks. It consists of multiple layers of interconnected nodes or neurons, where each neuron in one layer is connected to all the neurons in the next layer. The architecture of an FCNN can be represented mathematically by a set of weight matrices  $W_l$ , where  $l$  denotes the layer index. Each weight matrix represents the connections between the neurons in the previous layer and the current layer. The input to the first layer is usually a vector  $x \in R^n$  representing the features of the data sample. The output of the  $i$ -th neuron in the  $l$ -th layer can be calculated as:

$$z_i^l = \sigma\left(\sum_{j=1}^n w_{ij}^l a_j^{l-1} + b_i^l\right) \quad (1)$$

where  $\sigma$  is the activation function,  $a_j^{l-1}$  is the output of the  $j$ -th neuron in the previous layer,  $w_{ij}^l$  is the weight connecting the  $j$ -th neuron in the previous layer to the  $i$ -th neuron in the current layer, and  $b_i^l$  is the bias term associated with the  $i$ -th neuron in the current layer. The output of the last layer is usually interpreted as the prediction of the model for the given input.

## B Methodology

### B.1 Algorithm Description

We provide a pseudo-code describing our proposed model, as shown in the following Algorithm 1.

---

#### Algorithm 1 TrajectoryFlowNet

---

Initialize parameters  $\theta$  of the fully connected network  $\mathcal{N}_1$   
Initialize parameters  $\vartheta$  of the fully connected network  $\mathcal{N}_2$   
Define the training dataset:  $\{(x_0^i, y_0^i, t_0^i, \tau^i, t^i, u^i, v^i)\}_{i=1}^{N_d}$   
Define collocation points:  $\{(x_0^j, y_0^j, t_0^j, \tau^j, t^j)\}_{j=1}^{N_c}$   
Define Gaussian random matrix:  $\{B_1, B_2\}$

**while** not converged **do**

**for** each data point  $(x_0^i, y_0^i, t_0^i, \tau^i, u^i, v^i)$  **do**

    Compute Fourier features:

$$\gamma_1(\mathbf{v}_0^d) = [\cos(2\pi B_1 \mathbf{v}_0^d), \sin(2\pi B_1 \mathbf{v}_0^d)]^\top$$

where  $\mathbf{v}_0^d = [x_0^i, y_0^i, t_0^i, \tau^i]^\top$

    Predict displacement  $(\tilde{x}_q^i, \tilde{y}_q^i)$  using network  $\mathcal{N}_1$ :

$$\tilde{x}_q^i, \tilde{y}_q^i = \mathcal{N}_1(\gamma_1(\mathbf{v}_0^d); \theta)$$

    Compute the new positions:

$$x_q^i = x_0^i + \tilde{x}_q^i, \quad y_q^i = y_0^i + \tilde{y}_q^i$$

    Compute Fourier features:

$$\gamma_2(\mathbf{v}_q^d) = [\cos(2\pi B_2 \mathbf{v}_q^d), \sin(2\pi B_2 \mathbf{v}_q^d)]^\top$$

where  $\mathbf{v}_q^d = [x_q^i, y_q^i, t^i]^\top$

    Predict  $(\hat{u}^i, \hat{v}^i, \hat{p}^i)$  using network  $\mathcal{N}_2$ :

$$\hat{u}^i, \hat{v}^i, \hat{p}^i = \mathcal{N}_2(\gamma_2(\mathbf{v}_q^d); \vartheta)$$

**end for**

**for** each collocation point  $(x_0^j, y_0^j, t_0^j, \tau^j, t^j)$  **do**

    Compute Fourier features:

$$\gamma_1(\mathbf{v}_0^c) = [\cos(2\pi B_1 \mathbf{v}_0^c), \sin(2\pi B_1 \mathbf{v}_0^c)]^\top$$

where  $\mathbf{v}_0^c = [x_0^j, y_0^j, t_0^j, \tau^j]^\top$

Predict displacement  $(\tilde{x}_q^j, \tilde{y}_q^j)$  using network  $\mathcal{N}_1$ :

$$\tilde{x}_q^j, \tilde{y}_q^j = \mathcal{N}_1(\gamma_1(\mathbf{v}_q^c); \theta)$$

Compute the new positions:

$$x_q^j = x_0^j + \tilde{x}_q^j, \quad y_q^j = y_0^j + \tilde{y}_q^j$$

Compute Fourier features:

$$\gamma_2(\mathbf{v}_q^c) = [\cos(2\pi B_2 \mathbf{v}_q^c), \sin(2\pi B_2 \mathbf{v}_q^c)]^\top$$

where  $\mathbf{v}_q^c = [x_q^j, y_q^j, t^j]^\top$

Predict  $(\hat{u}^j, \hat{v}^j, \hat{p}^j)$  using network  $\mathcal{N}_2$ :

$$\hat{u}^j, \hat{v}^j, \hat{p}^j = \mathcal{N}_2(\gamma_2(\mathbf{v}_q^c); \vartheta)$$

Compute the time derivative of  $x_q^j$  and  $y_q^j$ :

$$\frac{\partial x_q^j}{\partial \tau^j}, \quad \frac{\partial y_q^j}{\partial \tau^j}$$

Compute the residuals of the non-dimensional Navier-Stokes equations:

$$R_x = \frac{\partial \hat{u}^j}{\partial t^j} + \hat{u}^j \frac{\partial \hat{u}^j}{\partial x_q^j} + \hat{v}^j \frac{\partial \hat{u}^j}{\partial y_q^j} - \text{Re} \left( \frac{\partial^2 \hat{u}^j}{\partial x_q^{j2}} + \frac{\partial^2 \hat{u}^j}{\partial y_q^{j2}} \right) + \frac{\partial \hat{p}^j}{\partial x_q^j}$$

$$R_y = \frac{\partial \hat{v}^j}{\partial t^j} + \hat{u}^j \frac{\partial \hat{v}^j}{\partial x_q^j} + \hat{v}^j \frac{\partial \hat{v}^j}{\partial y_q^j} - \text{Re} \left( \frac{\partial^2 \hat{v}^j}{\partial x_q^{j2}} + \frac{\partial^2 \hat{v}^j}{\partial y_q^{j2}} \right) + \frac{\partial \hat{p}^j}{\partial y_q^j}$$

**end for**

Compute total loss:

$$\mathcal{L} = \frac{1}{N_d} \sum_{i=1}^{N_d} \left( \left| x_q^i - x^i \right|^2 + \left| y_q^i - y^i \right|^2 + \left| \hat{u}^i - u^i \right|^2 + \left| \hat{v}^i - v^i \right|^2 \right)$$

$$+ \frac{1}{N_c} \sum_{j=1}^{N_c} \left( \left| \frac{\partial x_q^j}{\partial \tau^j} - \hat{u}^j \right|^2 + \left| \frac{\partial y_q^j}{\partial \tau^j} - \hat{v}^j \right|^2 + |R_x|^2 + |R_y|^2 \right)$$

Update the parameters of both networks:

$$\theta \leftarrow \theta - \eta \nabla_\theta \mathcal{L}, \quad \vartheta \leftarrow \vartheta - \eta \nabla_\vartheta \mathcal{L}$$

**end while** **return** the predicted fields  $(\hat{x}, \hat{y}, \hat{u}, \hat{v}, \hat{p})$

---

## B.2 Variables Notation

Moreover, we present a summary of the variable notations used in our paper, as detailed in Table S.1.

## C Dataset

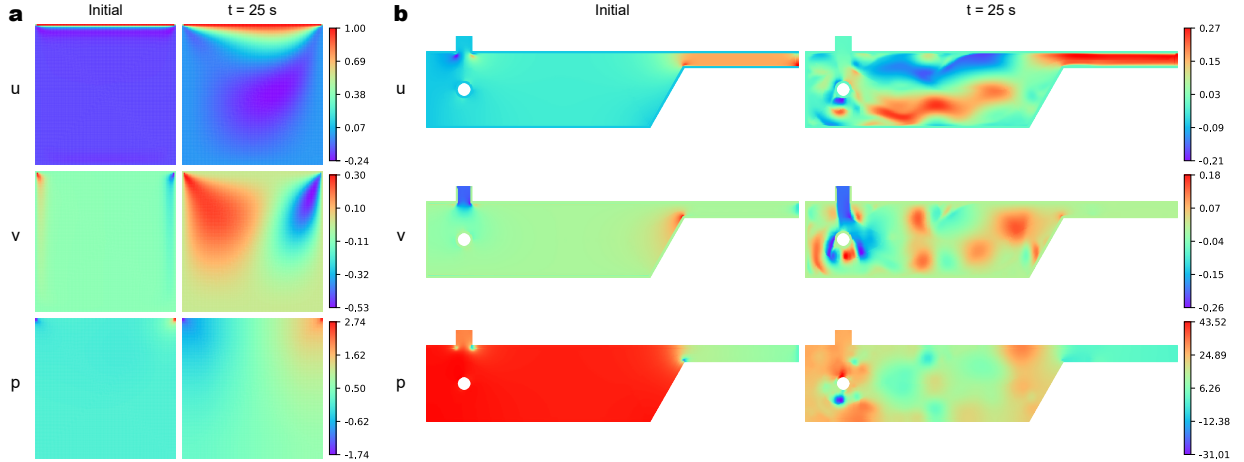
We evaluated the performance of our proposed method using two simulated datasets and two real experimental dataset. The simulated datasets were generated using ANSYS FLUENT, featuring a lid-driven cavity flow with closed boundaries and a complex cylinder flow characterized by open boundaries. The experimental dataset comprised measurements of aortic blood flow obtained from laboratory experiments. Each dataset was divided into separate training and testing sets to build the model. The model was trained on the training dataset and evaluated on the unseen testing dataset to assess its performance. Specific details regarding the number of particles in the training and testing sets for each scenario are provided in Table S.2. Notably, the experimental dataset included a large number of passive particles with short tracking durations; therefore, the table shows only particles that were tracked for more than two time steps. Despite this filtering, the testing set still represents 15 % of the total data volume used in the experiment.

**Table S.1:** Variables notation used in our paper.

Variable Name	Short Name	Role
space coordinate's initial x-position of the particle	$x_0$	Input
space coordinate's initial y-position of the particle	$y_0$	Input
particle's initial motion time under Euler description	$t_0$	Input
particle's motion time under Lagrangian description	$\tau$	Input
particle's motion time under Euler description	$t$	Input
reynolds number	$Re$	Input/Predicted
particle's x-direction of space coordinate	$x(x_0, y_0, t_0, \tau, t, Re)$	Input/Predicted
particle's y-direction of space coordinate	$y(x_0, y_0, t_0, \tau, t, Re)$	Input/Predicted
x-component of velocity	$u(x_0, y_0, t_0, \tau, t, Re)$	Input/Predicted
y-component of velocity	$y(x_0, y_0, t_0, \tau, t, Re)$	Input/Predicted
pressure	$p(x_0, y_0, t_0, \tau, t, Re)$	Predicted

**Table S.2:** Dataset Partitioning Based on Number of Tracked Particles.

Dataset	Lid-driven Cavity Flow	Complex Cylinder Flow	Experimental Aortic Blood Flow	Experimental LV Blood Flow
Training	200	2000	372	527
Testing	100	200	69	98

**Figure S.1:** The snapshots of datasets. **a**, The snapshots of Lid-driven Cavity Flow datasets. **b**, The snapshots of Complex Cylinder Flow datasets.

### C.1 Lid-driven Cavity Flow

The lid-driven cavity flow [2] is a classic fluid dynamics problem that includes various phenomena such as boundary layer separation, cavity vortices, and self-sustained oscillations. We created a square cavity with a side length of 1 using FLUENT, where the left, right, and bottom walls were fixed, while the top wall acted as a moving boundary. Initially, the top lid moved to the right at a velocity of  $u_0 = 1$ , resulting in a Reynolds number of 100 based on this velocity. The computational domain was discretized into a uniform grid of  $100 \times 100$ . Under the influence of the moving lid, a

large vortex formed near the geometric center of the cavity, with reduced flow at the bottom and side edges. At  $t = 3$  s, 300 particles were randomly distributed within the cavity, as illustrated in the figure, capturing their trajectories, velocities, and pressure values at their respective locations. From these, 200 particles were randomly selected for training, while another 100 non-overlapping particles were chosen for testing. The total simulation duration was 30 seconds. To enhance randomness in particle distribution, we focused on training and predicting the passive particle features only from the 22nd to 30th second. A snapshot of the flow field’s velocity and pressure at  $t = 25$  s is shown in Figure S.1. The L-BFGS optimization method was employed until convergence was achieved.

## C.2 Complex Cylinder Flow

Traditional studies typically focus on the wake region behind a single cylinder under simplified conditions. In contrast, our Complex Cylinder Flow dataset simulates a more intricate flow field around a cylinder with open boundaries, encompassing the entire flow region. To better match real-world conditions, we used water with properties closer to those found in practical scenarios, rather than idealized fluids, to achieve lower Reynolds numbers. This approach introduces additional complexities and provides a more realistic and challenging test case for evaluating our proposed method. The dataset was generated using ANSYS FLUENT to simulate liquid water with a density of approximately  $998.2 \text{ kg/m}^3$  and a viscosity of about  $0.001003 \text{ kg/(m} \cdot \text{s)}$ . Water was injected into the computational domain from the top inlet at a velocity of  $0.2 \text{ m/s}$ , with an outlet pressure set to  $0 \text{ Pa}$ . All passive tracer particles were released from the inlet to ensure a consistent particle concentration within the domain. The movement paths of the particles and their corresponding velocity and pressure values were recorded over a total duration of 30 seconds. However, for training and testing purposes, only data collected between  $24.5 \text{ s}$  and  $25.5 \text{ s}$  were utilized. From these, 2000 particles were randomly selected for training, and an additional 200 unique particles were chosen for testing. A snapshot of the flow field velocity and pressure at  $25 \text{ s}$  is shown in Figure S.1.

## C.3 Experimental Aortic Blood Flow

The aortic valve, situated between the left ventricle and the aorta, facilitates unidirectional blood flow into systemic circulation. Pathological calcification of the aortic valve leads to aortic stenosis (AS), a condition that affects  $2.8 \%$  of adults aged  $>75$  years, obstructing cardiac output and potentially causing fatal cardiovascular complications if left untreated. Transcatheter aortic valve replacement (TAVR) is a minimally invasive and worldwide adopted interventional treatment for aortic stenosis [12, 13]. Developed as an alternative to surgical aortic valve replacement (SAVR) for high-risk patients, TAVR deploys bioprosthetic valves via catheter. These valves are categorized into self-expanding valves (SEVs) with adaptive nitinol frames or balloon-expandable valves (BEVs), which require immediate circular expansion. While both valve types have been widely adopted, there is ongoing debate regarding their hemodynamic performance and long-term outcomes, with no definitive consensus on which valve type is superior. Our in vitro 3D particle image velocimetry study will quantify SEV/BEV flow fields, explaining mechanisms behind diagnostic discrepancies and guiding optimized valve selection.

A normal aortic root model without coronary connections was connected to a simulated circulatory loop driven by a pulsatile pump (Vivitro SuperPump, ViVitro Labs, Inc.). The silicone model with the left common carotid, left subclavian artery, and brachiocephalic artery was 3D-printed according to the CT data of a healthy person. Its refractive index is  $1.41$  and its thickness is  $2 \text{ mm}$ . In the test section, the aortic root model was immersed into an acrylic hydraulic chamber filled with working fluid. The inlet of the model was connected with the left ventricular compliance chamber,

and the model outlet was connected with the fluid reservoir. The blood analog was a mixture with 62 % water, 38 % glycerol by volume, and 229.22 g/L urea by weight was added into the solution to match the refractive index. The density and dynamic viscosity of the mixture were 1.3284 g/mL and 3.345 mPa · s, respectively, and the refractive index was 1.4108 at a working temperature of 26 °C. A 23 mm Edwards SAPIEN TAV was deployed at the annulus plane of the aortic root model. A clinician instructed the placement of the TAV. The valve position was secured using cable tie to prevent migration during pulsatile flow. A mechanical valve was used as a mitral valve within the ViVitro SuperPump. During systole, the blood analog flows from the left ventricular compliance chamber to the aortic root through the TAV, and then flow through the resistance valve, fluid reservoir and mitral valve back to left ventricle. Note that there is no blood flowing through the left common carotid, left subclavian artery and brachiocephalic artery. These vessels serve for fixation of the aortic root model during experiments. A resistance valve is used to adjust the systematic resistance. The fluid reservoir is open to the atmosphere to simulate the low pressure of the venous system. The flow downstream the TAV was measured under a physiological condition of 70 beats per minute and 7 L/min cardiac output. The systolic and diastolic aortic pressure are 110 mmHg and 45 mmHg, respectively. A time-resolved two-dimensional (2D) PIV experiment was conducted to measure the flow downstream the TAV along the centerline of the root. The flow motion was visualized by seeding 7  $\mu$ m fluorescent Rhodamine-B-coated particles with a density of 1500 kg/m<sup>3</sup> into the working fluid. These particles were excited using a laser sheet with a thickness of 1.0 mm, generated by a double-pulsed laser (Beamtech, Vlite-Hi-50) with a wavelength of 527 nm at a repetition rate of 0.2 kHz. A high-speed CMOS camera (VEO-440L-36G-M version) equipped with a 100 mm/f2.8 lens (Tokina atx-i) with a high-pass filter was used to capture the particle image pairs with resolution of 1664 × 1660 pixels. The acquisition frequency is 200 Hz, and the time separation was set to 400  $\mu$ s. The digital resolution of the images was 12.31 pixels/mm, therefore, the maximum displacement was less than 15 pixels according to the maximum velocity of 3 m/s at peak systole. Manual tracking of particle positions over time was also performed.

The particle image pairs were processed using an in-house PIV software with a three-pass window deformation iterative multigrid scheme [14, 15]. Before velocity calculation, image preprocess with sliding minimum was performed to remove the image background. The final interrogation window size was 16 × 16 pixels with 50 % overlap, and the vectors at the final pass were Gaussian filtered with the same sizes the interrogation window to reduce the random noise. This configuration yielded a spatial resolution of 1.3 mm with a vector interval of 0.65 mm. The edge of aortic root was identified according to the image intensity gradient and converted to physical coordinates based on the calibration. Particle data, a mix of manually tracked and PIV software-processed data, was used to simulate trajectories of particles moving over different time spans. In the dataset, 80 % of the total available data comprised the training set, while 15 % formed the test set.

## C.4 Experimental Left Ventricle Blood Flow

The mitral valve, situated between the left atrium and ventricle, ensures unidirectional blood flow from the atrium to the ventricle [16]. In a normal mitral valve, intraventricular flow patterns exhibit physiological vortex dynamics that pump blood out of the left ventricle in an energy-efficient manner. Intraventricular hemodynamics is intricately linked to ventricular vortices and flow-induced stresses, which regulate the balance between hemodynamic load and myocardial stress [17]. This balance interfaces with biochemical pathways involving genes critical for cardiovascular morphogenesis, ultimately driving processes such as left ventricular remodeling. Consequently, analyzing left ventricular flow fields under physiological mitral valve conditions is essential for understanding their functional implications on cardiac performance.

For the experiment, the aortic root, aortic valve, and the complete mitral valve complex, including the annulus, anterior and posterior leaflets, chordae tendineae, and papillary muscles, were surgically dissected and sutured onto a 3D-printed annular resin plate connected to a silicone left ventricle. The geometry of the silicone left ventricle was reconstructed from adult heart CT data, with a wall thickness of 2 mm and a refractive index of 1.4.

The mitral valve-silicone left ventricle assembly was placed in a nine-sided chamber filled with a glycerol-water solution consisting of 62 % water and 38 % glycerol by volume. The solution had a dynamic viscosity of  $3.49 \text{ mPa} \cdot \text{s}$  at a temperature of  $26.9^\circ\text{C}$ . A piston driven by an electric motor generated periodic compression and relaxation of the chamber fluid to simulate left ventricular systole and diastole at a heart rate of 60 beats per minute and a cardiac output of 3.6 liters per minute. The fluid circulated in a closed loop, passing through the left ventricle, aortic valve, aortic compliance chamber, resistance valves, reservoir, left atrium, and mitral valve.

Fluorescent tracer particles coated with Rhodamine B, with an average diameter of 7 microns, a density of  $1500 \text{ kg/m}^3$ , and a response frequency of 854.7 Hz, were uniformly distributed in the flow field. A double-pulsed laser system, model Vlite-Hi-527-50 from Beijing Laser Optoelectronics Technology Co., Ltd., with a wavelength of 527 nm, a repetition rate of 200 Hz, and a pulse interval optimized to ensure displacement less than 8 pixels, generated a light sheet with a thickness of 1.0 mm. The emitted fluorescence at 590 nm was captured by a high-speed camera, model Imager HS from LaVision GmbH, equipped with a Tokina 100 mm/f2.8 fixed-focus lens and an optical filter with transmission greater than 90 % for wavelengths above 570 nm. The image resolution was  $2016 \times 2016$  pixels, with 20 pixels per millimeter. Velocity fields were calculated using a window deformation iterative multigrid scheme, with two iterations and a final interrogation window size of  $32 \times 32$  pixels overlapped by 75 %. Outliers were removed using normalized median tests, achieving a vector spacing of 0.4 mm and a spatial resolution of 1.6 mm. Gaussian smoothing was applied to enhance the visualization of flow structures, while particle trajectories were manually tracked.

## D Results

Our model utilizes the Limited-memory Broyden-Fletcher-Goldfarb-Shanno (LBFGS) optimizer [6] with consistent parameter settings across all models. The optimizer is configured with a learning rate of 1.0, maximum iterations set to 500,000, maximum function evaluations limited to 500,000, a history size of 50, tolerance for gradient convergence at  $1e-5$ , tolerance for change in function value at 1.0 times the machine epsilon, and employs the strong Wolfe line search method. The hyperparameters of the model are uniformly set to 1.0. Training proceeds until convergence is achieved or a predefined stopping criterion is met.

### D.1 Fourier feature mapping

The method of Fourier feature mapping (FFM) was employed in our article. Before inputting parameters into the neural network, Fourier feature mapping was used to characterize the input parameters, enabling better capture of high-frequency features during the prediction process.

All cases were sampled using Gaussian random sampling. For Lid-Driven Cavity Flow, each entry in  $\mathbf{B} \in \mathbb{R}^{50 \times d}$  is sampled from  $\mathcal{N}(0, 0.1)$ , and for the other two cases, each entry in  $\mathbf{B} \in \mathbb{R}^{500 \times d}$  is sampled from  $\mathcal{N}(0, 1)$ . In all cases,  $d = 4$  for  $\mathcal{N}_1$  and  $d = 3$  for  $\mathcal{N}_2$ .

We compared the impact of using Fourier features on the prediction results, as shown in Table S.3. The results indicate that using this method maintains good prediction accuracy across all test results.



**Table S.3:** Comparison of Prediction Accuracy with and without Fourier Feature Mapping.

Case	Method	Error			
		$x$	$y$	$u$	$v$
Lid-driven	Without FFM	$3.00 \times 10^{-3}$	$3.42 \times 10^{-3}$	$6.44 \times 10^{-2}$	$6.57 \times 10^{-2}$
Cavity Flow	With FFM	<b><math>2.93 \times 10^{-3}</math></b>	<b><math>2.18 \times 10^{-3}</math></b>	<b><math>4.05 \times 10^{-2}</math></b>	<b><math>4.56 \times 10^{-2}</math></b>
Complex Cylinder	Without FFM	$4.28 \times 10^{-2}$	$8.68 \times 10^{-2}$	$2.81 \times 10^{-1}$	$2.93 \times 10^{-1}$
Flow Field	With FFM	<b><math>2.46 \times 10^{-2}</math></b>	<b><math>8.06 \times 10^{-2}</math></b>	<b><math>2.25 \times 10^{-1}</math></b>	<b><math>2.42 \times 10^{-1}</math></b>
Experimental	Without FFM	$7.52 \times 10^{-3}$	$3.60 \times 10^{-3}$	$4.97 \times 10^{-1}$	$6.30 \times 10^{-1}$
Aortic Blood Flow	With FFM	<b><math>2.40 \times 10^{-3}</math></b>	<b><math>1.86 \times 10^{-3}</math></b>	<b><math>2.90 \times 10^{-1}</math></b>	<b><math>4.01 \times 10^{-1}</math></b>
Experimental	Without FFM	$4.08 \times 10^{-2}$	<b><math>7.21 \times 10^{-2}</math></b>	$8.73 \times 10^{-1}$	$6.92 \times 10^{-1}$
LV Blood Flow	With FFM	<b><math>1.52 \times 10^{-2}</math></b>	$9.04 \times 10^{-2}$	<b><math>6.20 \times 10^{-1}</math></b>	<b><math>3.64 \times 10^{-1}</math></b>

## D.2 Impact of Physical Constraints

In this section, we compare the algorithm presented in the paper with methods that use different networks to independently predict the trajectories of passive particles and flow field information. For the separate prediction methods, we ensure that there is no connection between network Trajectory block and Flow Field block, while keeping the input and output of Trajectory block and Flow Field block the same as in the algorithm described in the paper. However, the separately trained Trajectory block does not have physical constraints, whereas Flow Field block includes NS equation constraints. All other settings remain consistent with the algorithm in the paper. The results are shown in Table S.4. In most cases, our algorithm performs better on the test set compared to separate prediction methods. However, it is important to note that our algorithm is sensitive to the prediction of passive particle trajectories. Specifically, if the trajectory prediction is inaccurate, it can reduce the accuracy of subsequent flow field predictions.

**Table S.4:** Comparison of performance metrics between TrajectoryFlowNet and separate training methods.

Case	Method	Error			
		$x$	$y$	$u$	$v$
Lid-driven	Separate Training	$1.78 \times 10^{-2}$	$1.21 \times 10^{-2}$	$4.70 \times 10^{-2}$	$4.72 \times 10^{-2}$
Cavity Flow	TrajectoryFlowNet	<b><math>2.93 \times 10^{-3}</math></b>	<b><math>2.18 \times 10^{-3}</math></b>	<b><math>4.05 \times 10^{-2}</math></b>	<b><math>4.56 \times 10^{-2}</math></b>
Complex Cylinder	Separate Training	$3.35 \times 10^{-2}$	<b><math>7.70 \times 10^{-2}</math></b>	<b><math>1.71 \times 10^{-1}</math></b>	<b><math>1.86 \times 10^{-1}</math></b>
Flow Field	TrajectoryFlowNet	<b><math>2.46 \times 10^{-2}</math></b>	$8.06 \times 10^{-2}$	$2.25 \times 10^{-1}$	$2.42 \times 10^{-1}$
Experimental	Separate Training	$9.84 \times 10^{-3}$	$4.69 \times 10^{-3}$	$4.18 \times 10^{-1}$	$5.35 \times 10^{-1}$
Aortic Blood Flow	TrajectoryFlowNet	<b><math>2.40 \times 10^{-3}</math></b>	<b><math>1.86 \times 10^{-3}</math></b>	<b><math>2.90 \times 10^{-1}</math></b>	<b><math>4.01 \times 10^{-1}</math></b>
Experimental	Separate Training	$1.72 \times 10^{-2}$	$1.00 \times 10^{-1}$	$6.52 \times 10^{-1}$	$3.86 \times 10^{-1}$
LV Blood Flow	TrajectoryFlowNet	<b><math>1.52 \times 10^{-2}</math></b>	<b><math>9.04 \times 10^{-2}</math></b>	<b><math>6.20 \times 10^{-1}</math></b>	<b><math>3.64 \times 10^{-1}</math></b>

## D.3 Activation function

In this section, we conducted tests on various activation functions, including the Rectified Linear Unit (ReLU) [8], Exponential Linear Unit (ELU) [9], Hyperbolic Tangent (Tanh) [10], and Sigmoid [11]. The effectiveness of these activation functions was evaluated based on the total sum of relative L2 errors from the test set, as shown in Table S.5. It is worth noting that the only

difference between the different test models lies in the choice of activation function, as all models were trained using the L-BFGS optimizer until convergence. The experimental results consistently demonstrated that the Tanh activation function outperformed others across all datasets. Therefore, we consider Tanh to be a suitable and widely applicable choice for the majority of datasets in this study.

**Table S.5:** Evaluation of Activation Functions based on Relative L2 Errors in Test Set.

Case	Activation Function	Error			
		$x$	$y$	$u$	$v$
Lid-driven Cavity Flow	ReLU	$8.19 \times 10^{-2}$	$1.00 \times 10^{-1}$	$6.83 \times 10^{-1}$	$7.62 \times 10^{-1}$
	ELU	$2.49 \times 10^{-2}$	$2.82 \times 10^{-2}$	$7.62 \times 10^{-1}$	$2.66 \times 10^{-1}$
	Tanh	<b><math>2.93 \times 10^{-3}</math></b>	<b><math>2.18 \times 10^{-3}</math></b>	<b><math>4.05 \times 10^{-2}</math></b>	<b><math>4.56 \times 10^{-2}</math></b>
	Sigmoid	$5.23 \times 10^{-1}$	$5.29 \times 10^{-1}$	$1.00 \times 10^0$	$1.00 \times 10^0$
Complex Cylinder Flow Field	ReLU	$3.77 \times 10^{-2}$	$1.34 \times 10^{-1}$	$4.42 \times 10^{-1}$	$7.20 \times 10^{-1}$
	ELU	$3.10 \times 10^{-2}$	$9.18 \times 10^{-2}$	$3.52 \times 10^{-1}$	$5.97 \times 10^{-1}$
	Tanh	<b><math>2.46 \times 10^{-2}</math></b>	<b><math>8.06 \times 10^{-2}</math></b>	<b><math>2.25 \times 10^{-1}</math></b>	<b><math>2.42 \times 10^{-1}</math></b>
	Sigmoid	$1.99 \times 10^{-1}$	$4.17 \times 10^{-1}$	$1.00 \times 10^0$	$9.99 \times 10^{-1}$
Experimental Aortic Blood Flow	ReLU	$1.98 \times 10^{-2}$	$1.54 \times 10^{-2}$	$9.99 \times 10^{-1}$	$9.99 \times 10^{-1}$
	ELU	$7.65 \times 10^{-3}$	$5.62 \times 10^{-3}$	$6.23 \times 10^{-1}$	$7.45 \times 10^{-1}$
	Tanh	<b><math>2.40 \times 10^{-3}</math></b>	<b><math>1.86 \times 10^{-3}</math></b>	<b><math>2.90 \times 10^{-1}</math></b>	<b><math>4.01 \times 10^{-1}</math></b>
	Sigmoid	$1.56 \times 10^{-1}$	$4.01 \times 10^{-2}$	$1.00 \times 10^0$	$1.00 \times 10^0$
Experimental LV Flow	ReLU	$2.74 \times 10^{-2}$	<b><math>6.85 \times 10^{-2}</math></b>	$9.98 \times 10^{-1}$	$9.97 \times 10^{-1}$
	ELU	<b><math>1.38 \times 10^{-2}</math></b>	$7.27 \times 10^{-2}$	<b><math>6.01 \times 10^{-1}</math></b>	$3.75 \times 10^{-1}$
	Tanh	$1.52 \times 10^{-2}$	$9.04 \times 10^{-2}$	$6.20 \times 10^{-1}$	<b><math>3.64 \times 10^{-1}</math></b>
	Sigmoid	$1.27 \times 10^{-1}$	$1.72 \times 10^{-1}$	$1.00 \times 10^0$	$1.00 \times 10^0$

## Supplementary References

- [1] Yann LeCun, Yoshua Bengio, and Geoffrey Hinton. Deep learning. *nature*, 521(7553):436–444, 2015.
- [2] O Botella and R Peyret. Benchmark spectral results on the lid-driven cavity flow. *Computers & Fluids*, 27(4):421–433, 1998.
- [3] Karl Perktold and Martin Prosi. Computational models of arterial flow and mass transport. In *Cardiovascular fluid mechanics*, pages 73–136. Springer, 2003.
- [4] Jerry Westerweel, Gerrit E Elsinga, and Ronald J Adrian. Particle image velocimetry for complex and turbulent flows. *Annual Review of Fluid Mechanics*, 45(1):409–436, 2013.
- [5] Wei-Liem Loh. On latin hypercube sampling. *The annals of statistics*, 24(5):2058–2080, 1996.
- [6] Dong C Liu and Jorge Nocedal. On the limited memory bfgs method for large scale optimization. *Mathematical programming*, 45(1):503–528, 1989.
- [7] Dumitru Erhan, Aaron Courville, Yoshua Bengio, and Pascal Vincent. Why does unsupervised pre-training help deep learning? In *Proceedings of the thirteenth international conference on artificial intelligence and statistics*, pages 201–208. JMLR Workshop and Conference Proceedings, 2010.
- [8] Kazuyuki Hara, Daisuke Saito, and Hayaru Shouno. Analysis of function of rectified linear unit used in deep learning. In *2015 international joint conference on neural networks (IJCNN)*, pages 1–8. IEEE, 2015.

- [9] Djork-Arné Clevert, Thomas Unterthiner, and Sepp Hochreiter. Fast and accurate deep network learning by exponential linear units (elus). *arXiv preprint arXiv:1511.07289*, 2015.
- [10] Chigozie Nwankpa, Winifred Ijomah, Anthony Gachagan, and Stephen Marshall. Activation functions: Comparison of trends in practice and research for deep learning. *arXiv preprint arXiv:1811.03378*, 2018.
- [11] Jun Han and Claudio Moraga. The influence of the sigmoid function parameters on the speed of backpropagation learning. In *International workshop on artificial neural networks*, pages 195–201. Springer, 1995.
- [12] Yuki Takahashi, Kiwamu Kamiya, Toshiyuki Nagai, Satonori Tsuneta, Noriko Oyama-Manabe, Takeshi Hamaya, Sho Kazui, Yutaro Yasui, Kohei Saiin, Seiichiro Naito, et al. Differences in blood flow dynamics between balloon- and self-expandable valves in patients with aortic stenosis undergoing transcatheter aortic valve replacement. *Journal of Cardiovascular Magnetic Resonance*, 25(1):60, 2023.
- [13] Jianming Li, Wentao Yan, Wenshuo Wang, Shengzhang Wang, and Lai Wei. Comparison of balloon-expandable valve and self-expandable valve in transcatheter aortic valve replacement: A patient-specific numerical study. *Journal of Biomechanical Engineering*, 144(10):104501, 2022.
- [14] Fulvio Scarano. Iterative image deformation methods in piv. *Measurement science and technology*, 13(1):R1, 2001.
- [15] Hongping Wang, Guowei He, and Shizhao Wang. Globally optimized cross-correlation for particle image velocimetry. *Experiments in Fluids*, 61:1–17, 2020.
- [16] Karen P McCarthy, Liam Ring, and Bushra S Rana. Anatomy of the mitral valve: understanding the mitral valve complex in mitral regurgitation. *European Journal of echocardiography*, 11(10):i3–i9, 2010.
- [17] Jay R Hove, Reinhard W Köster, Arian S Forouhar, Gabriel Acevedo-Bolton, Scott E Fraser, and Morteza Gharib. Intracardiac fluid forces are an essential epigenetic factor for embryonic cardiogenesis. *Nature*, 421(6919):172–177, 2003.